Current Research in Biotechnology 7 (2024) 100176

Contents lists available at ScienceDirect

Current Research in Biotechnology

journal homepage: www.elsevier.com/locate/crbiot

Favipiravir *vs.* Deferiprone: Tautomeric, photophysical, *in vitro* biological studies, and binding interactions with SARS-Cov-2-M^{Pro}/ACE2

Nikolay T. Tzvetkov [a,*], Martina I. Peeva [a], Maya G. Georgieva [a], Vera Deneva [b,c], Aneliya A. Balacheva [a], Ivan P. Bogdanov [a], Maria Ponticelli [d], Luigi Milella [d,e], Kiril Kirilov [a,f], Maima Matin [g], Hans-Georg Stammler [h], Atanas G. Atanasov [g,i], Liudmil Antonov [b]

[a] *Department of Biochemical Pharmacology and Drug Design, Institute of Molecular Biology "Roumen Tsanev", Bulgarian Academy of Sciences, Acad. G. Bonchev Str., bl. 21, 1113 Sofia, Bulgaria*
[b] *Institute of Electronics, Bulgarian Academy of Sciences, 1784 Sofia, Bulgaria*
[c] *Institute of Organic Chemistry with Centre of Phytochemistry, Bulgarian Academy of Sciences, 1113 Sofia, Bulgaria*
[d] *Department of Science, University of Basilicata, V.le dell'Ateneo Lucano 10, 85100 Potenza, Italy*
[e] *Spinoff Bioactiplant, V.le dell'Ateneo Lucano 10, 85100 Potenza, Italy*
[f] *Department of Natural Sciences, New Bulgarian University, 21 Montevideo Str., Sofia 1618, Bulgaria*
[g] *Institute of Genetics and Animal Biotechnology of the Polish Academy of Sciences, Jastrzebiec, 05-552 Magdalenka, Poland*
[h] *Department of Chemistry, University of Bielefeld, Universitätsstr. 25, 33615 Bielefeld, Germany*
[i] *Ludwig Boltzmann Institute Digital Health and Patient Safety, Medical University of Vienna, Spitalgasse 23, 1090 Vienna, Austria*

ARTICLE INFO

Keywords:
Favipiravir
Deferiprone
Tautomer-based drug design
COVID-19
Molecular modelling
Tautomerism

ABSTRACT

Coronavirus disease 2019 (COVID-19) still remains the most disastrous infection continuously affecting millions of people worldwide. Herein, we performed a comparative study between the anti-influenza drug favipiravir (FAV) and the anti-thalassemia drug deferiprone (DFP) in order to examine their potential as basic scaffolds for the generation of most effective and structurally novel antivirals. To conduct the initial molecular modelling and virtual screening steps, our recently proposed single crystal X-ray diffraction (SCXRD)/HYdrogen DEssolvation (HYDE) technology platform has been used. This platform allows molecular design, interactive prioritization and virtual evaluation of newly designed molecules, simultaneously affecting two COVID-related targets, including angiotensin-converting enzyme 2 (ACE2) as a host-cellular receptor (*host-based approach*) and the main protease (M^{pro}) enzyme of the spike glycoprotein of SARS-Cov-2 (*virus-based approach*). Based on the molecular docking results, DFP has shown higher binding affinity ($K_{i\ HYDE}$ values) over FAV towards both biological targets. The tautomeric, physicochemical, and biological properties of FAV and DFP have been studied both experimentally and theoretically using molecular spectroscopy (UV–VIS absorption), parallel artificial membrane permeability assay, and cell biology (PAMPA and MTT assay), as well as DFT quantum chemical calculations. According to the obtained results, the enol tautomers of both compounds are considerably more stable in different organic solvents. However, the keto tautomer of FAV was estimated to be most preferable under physiological conditions, which is in good agreement with the molecular docking studies. The isolated crystal structure of DFP is in an excellent agreement with the computation in respect of the most stable tautomer. Combined single X-ray/molecular modeling studies including HYDE analyses provided not only insights into the protein–ligand interactions within the binding site of SARS-Cov-2-ACE2 and SARS-Cov-2-M^{pro}, but also a valuable information regarding the most stable enol tautomeric form of DFP that contributes to its estimated higher potency against these targets.

Abbreviations: ACE2, angiotensin-converting enzyme 2; ACN, acetonitrile; ADME-T, absorption, distribution, metabolism, excretion, and toxicity; BBB, blood–brain barrier; CNS, central nervous system; DEF, deferiprone; DFT, density functional theory; DMSO, *N*,*N*-dimethyl sulfoxide; EMA, European Medicine Agency; ESIPT, excited state intramolecular proton transfer; FAV, favipiravir; FBS, fetal bovine serum; FDA, U.S. Food and Drug Administration; GSIPT, ground state intramolecular proton transfer; HEPES, 2-[4-(2-hydroxyethyl)piperazin-1-yl)]ethane-1-sulfonic acid; hERG, human ether-a-go-go-related gene; HYDE, HYdrogen DEssolvation; LQTS, long QT syndrome; M^{pro}, main protease enzyme; MeOH, methanol; MTT, 3-(4,5-dimethylthiazol-2-yl)-2,5-diphenyltetrazolium bromide; PAMPA, parallel artificial membrane permeability assay; PBS, phosphate-buffered saline; PES, potential energy surface; RBD, receptor-binding domain; RdRp, RNA-dependent RNA polymerase; SARS-Cov-2, severe acute respiratory syndrome coronavirus 2; WHO, World Health Organization.

* Corresponding author.
E-mail address: ntzvetkov@bio21.bas.bg (N.T. Tzvetkov).

https://doi.org/10.1016/j.crbiot.2024.100176
Received 22 October 2023; Received in revised form 26 December 2023; Accepted 4 January 2024
Available online 8 January 2024

Introduction

The development of novel, multi-target anti-viral drugs with two or more pharmacophore units into a single molecule, simultaneously affecting two or more biological targets of interest, still remain a significant challenge for modern pharmaceutical research (Li et al., 2021; Anighoro et al., 2014). The coronavirus disease 2019 (COVID-19), caused by severe acute respiratory syndrome coronavirus 2 (SARS-Cov-2), has already infected ~ 670 million people worldwide with approximately seven million deaths (WHO Coronavirus (COVID-19) Dashboard) (Pozzi et al., 2023). It is one of the largest infections in this century with enormous health, social and economic impact on the communities around the world. As a consequence of the pandemic, enormous efforts have been made to develop new vaccines (mostly nucleoside-modified mRNA- and vector-based vaccines) against COVID-19, and a number of approved drugs, including small molecules (Galindez et al., 2021; Hu et al., 2021; Liu et al., 2021; Ghosh et al., 2020; Kupferschmidt and Cohen, 2020; Wang et al., 2020) and peptides (Wang et al., 2021; Maas et al., 2021; Sadremomtaz et al., 2022) have been investigated in order to find effective antivirals that can be applied immediately to treat infected patients.

Considering the enormous number of coronaviruses and their mutations, there are many strategies to design antiviral agents, especially against the SARS-Cov-2 variants (Liu et al., 2021; Sadremomtaz et al., 2022). These strategies involved *virus-based approaches* assessing available/existing antiviral and/or non-antiviral drugs (Liu et al., 2021), virtual (computational) screening of existing molecules (Galindez et al., 2021; Sadremomtaz et al., 2022; Aronskyy et al., 2021; Hufsky, 2021), designing of compounds that are able to block viral RNA synthesis (viral replication) (V'kovski, P., Kratzel, A., Steiner, S., Stalder, H., Thiel, V., 2021; Jin, 2020; Zhang et al., 2020) or to block the binding of the virus to specific human cell receptors (Yan et al., 2020; Lan et al., 2020). Other strategies include *host-based approaches* such as targeting of virus-specific human receptors or/and enzymes to develop selective drugs or vaccines (Wang et al., 2020; Wang et al., 2021; Maas et al., 2021; Sadremomtaz et al., 2022; Choudhary et al., 2020; Gil et al., 2020; Shur et al., 2020), and applying of variable computational genomic and pathological investigations on different COVID-19 variants to design new drugs (Galindez et al., 2021; Shur et al., 2020; VanPatten et al., 2020). There are two well-characterized drug targets considered for rapid development of SARS-Cov-2 antivirals. The first one is the main protease M^{pro} (also known as 3C-like protease, $3CL^{pro}$) representing the *virus-based approach* (Zhang et al., 2020; Choudhary et al., 2020; Gil et al., 2020), while the second one is the human angiotensin-converting enzyme 2 (hACE2) that covers the *host-based approach* (Kupferschmidt and Cohen, 2020; Gil et al., 2020; Shur et al., 2020). Along with a second papain-like protease (PL^{pro}), the main protease M^{pro} plays an essential role for replication of SARS-Cov-2 (Zhang et al., 2020). The human ACE2, is a type I cell membrane protein that relates to the entry of the coronaviruses into host cells via their viral spike (S) glycoprotein trimer. During viral infection, the S protein is cleaved by host proteases into S1 and S2 subunits (Hu et al., 2021; Maas et al., 2021; Yan et al., 2020). While the S1 subunit of the transmembrane glycoprotein selectively binds the protease domain (PD) of host cell receptor ACE2 via virus-specific receptor-binding domain (RBD), the S2 is responsible for membrane fusion that is crucial for host infection (Yan et al., 2020). Current investigations of the SARS-Cov-2 RBD-hACE2 complex have shown that the RBD of SARS-Cov-2 S protein predominantly binds with high affinity to the key α1-helix (of PD) of hACE2 (dissociation constant K_d of 14.7 nM) (Yan et al., 2020; Wrapp et al., 2020). In addition, the obtained X-ray and cryo-electron microscopic (cryo-EM) structures of SARS-Cov-1 (Tai et al., 2020) and SARS-Cov-2 (Lan et al., 2020; Wrapp et al., 2020) S-RBDs bound to ACE2, as well as the X-ray structures of M^{pro} from SARS-Cov-1 (Xue, 2007) and SARS-Cov-2 (Jin, 2020), represent the basis for rapid structure-based design of effective antivirals.

Despite the enormous efforts in the treatment and prevention/control (vaccination) of SARS-Cov-2 infections, there is an urgent need of antivirals with new mechanism of action that are able to effectively treat infections caused by coronavirus pathogens. Some of the approved by the WHO (including national and international Drug Agencies, such as FDA and EMA) medicines for emergency use to treat COVID-19 patients are already known antivirals developed for the treatment of various viral infections (Wang et al., 2020). The chemical structures of some investigational and approved Covid-19 antivirals are presented in Fig. 1. For example, the purine nucleoside prodrug AT-527 (Bemnifosbuvir, Atea Pharmaceuticals) (Good et al., 2021) and the serine protease inhibitor Nafamostat, which is widely used for the treatment of intravascular coagulation and pancreatitis (Zhuravel, 2021), are currently in Phase III clinical trials for treatment of COVID-19 (Fig. 1, in blue). Similar to AT-527, the ribonucleoside analog prodrug MK-4482 (Molnupiravir, brand name Lagevrio® MSD/Ridgeback; first oral antiviral agent for the treatment of COVID-19) (Holman, 2021) inhibit viral RNA replication demonstrating good tolerability and safety in clinical trials (Willyard, 2021), while the currently approved drug PF-07321332 (nirmatrelvir, brand name Paxlovid®, Pfizer) is an inhibitor of 3-chymotrypsin-like protease ($3CL^{pro}$, called also main protease M^{pro}) (Halford, 2021; Hammond, 2022).

The most prominent and widely used anti-COVID-19 agent is the nucleoside analog and prodrug Remdesivir (brand name Veklury®, Gliead Sciences Inc.) that inhibits viral RNA polymerases and thus viral replication (Wang, 2020; Beigel, 2020) (for approved drug, see Fig. 1, in red). All these compounds are small molecules (molecular weight between ~ 260 and ~ 600 Da) developed either as viral RNA-dependent RNA polymerase (RdRp) or main protease ($3CL^{pro}$/M^{pro}) inhibitors to block SARS-Cov-2 replication in host cells (*virus-based approach*). Among all approved drugs, the selective viral RdRp inhibitor Favipiravir (T-705, FAV, brand name Avigan®) is the smallest molecule (MW of 157 Da) used in the treatment of COVID-19 so far (*cf.* Fig. 1, cmpd. **1**) (Shiraki and Daikoku, 2020; Kostadinova et al., 2022; Rattanaumpawan et al., 2022). Similar to some antivirals, favipiravir (FAV, **1**) is a prodrug that is metabolized *in vivo* into its active form (Jin et al., 2013; Du and Chen, 2020) and that was initially developed as a broad-spectrum antiviral for the treatment of other pathogens, for example, influenza virus infections (Shiraki and Daikoku, 2020). In 2014 FAV was approved in Japan for the treatment or re-emerging of influenza viruses and in Russia, China, India, and other countries in 2020, for emergency use to treat SARS-Cov-2 patients (Shiraki and Daikoku, 2020; Rattanaumpawan et al., 2022; Deneva et al., 2023). Compared to other antivirals, FAV exhibits rich tautomeric functionality ('keto-enol' tautomerism), which allows, through structural modifications, to manipulate the tautomeric 'keto-enol' state and the shape of the molecule that could lead to a change in biological activity (Deneva et al., 2023; Antonov, 2020; Antonov, 2020). As approved for clinical use, FAV shows reduced number of side effects. In addition, FAV is easily available, chemically stable compound and, therefore, may be considered for further structural modifications in order to design new FAV-modified small molecules targeting viral proteins. Along with FAV (**1**), Deferiprone (DFP, brand name Ferriprox®) is another small compound that has attracted our attention as potential antiviral drug candidate against coronavirus infections (*cp.* Fig. 1, compound **2**). Deferiprone is an iron chelator approved by the EMA in 1994 and the FDA in 2021 to treat iron overload in patients with thalassemia major (Habib et al., 2021). Recent investigations have shown that iron overload is involved as a main contributor to the pathogenesis of COVID-19 infections (Habib et al., 2021; Liu and Li, 2020). This is not surprising because the key pathogenic molecular step of COVID-19 infections is to attack hemoglobin leading to loss of its capacity to bind with oxygen (Liu and Li, 2020). As a result, a dissociation of the porphyrins from iron with subsequent iron release into the circulations occurs (Habib et al., 2021; Liu and Li, 2020). The free iron overload (>300 μg/L) is thus associated with hindered oxygen delivery to the lungs and other major organs causing rapid oxidative damage (Liu and

Li, 2020; Kontoghiorghes, 2022). The potential use of DFP as an antiviral drug represents a new approach in the fight against SARS-Cov infections combining both, iron chelating activity with probable inhibiting efficacy against viral targets. Similar to FAV, DFP belongs to the low-molecular drugs (MW of 139 Da) comprising one mono-heterocyclic moiety (pyridine for DFP *vs.* pyrazine for FAV), which makes FAV and DFP accessible for further structural modifications in order to gain new antivirals.

The investigation of the tautomerism of antiviral (FAV, **1**) and non-antiviral (DFP, **2**) drugs alone and, on this basis, to perform *tautomer-based drug design* (Tzvetkov et al., 2016) of novel structures originating from drug's basic scaffold is conceptually novel approach (called *virus-host-multi-targeting approach*) used herein in the development of new antivirals (see Figure S1). Therefore, the aim of the current study was to investigate, for the first time, the spectral, *in vitro* properties, and tautomer distribution in solution of DFP (**2**) in comparison to FAV (**1**) as a representative for an already approved COVID-19 antiviral agent. In this work, we performed molecular docking studies (prediction of biological activity towards M^{pro} and hACE2 with subsequent thermodynamic analysis), UV–VIS spectroscopy, quantum-chemical calculations, and *in vitro* biological and physicochemical studies (cytotoxicity, PAMPA and *in silico* ADME-Tox parameters). Using the 3D-structure of FAV and the X-ray crystal structure of DFP as a template, we considered the energetics of their neutral and ionized species for computations. In addition, we compared the results obtained from the theory and optical spectra in order to determine the most stable tautomers of FAV and DFP in solution, and on this basis to propose new antiviral agents.

Results and discussion

X-ray structure of deferiprone (2)

The obtained X-ray structure of DFP (**2**) revealed that the ligand crystalized in a dimeric unit consisting of two neutral molecules of 3-hydroxy-1,2-dimethylpyridin-4(1*H*)-one (**2**) within a monoclinic system space group $P2_1/c$ (for details, see also the ORTEP diagram in Figure S2 and Table S1). The crystal packing can be described as alternating layers along the *a*-axis, in which two molecules are dimerized by forming hydrogen bonds between both enolic groups of **2** (O1-H1…O2) with a distance of 1.86(6) Å (Fig. 2). Moreover, the arrangement of each molecule between the layers induces weak intermolecular interactions formed via π-π staking of the pyridine ring (C1-C5-N1). The shortest centroid–centroid distance between the pyridine rings is 3.657(1) Å (Fig. 2).

Molecular docking studies with favipiravir (1) and deferiprone (2)

Following our *dual virus-host-targeting* approach for tautomer-based drug design of new antivirals, we performed extended docking experiments with both proposed compounds for further investigations, namely the small-molecule drugs FAV and DFP. In this context, the 3D-structure of FAV (**1**, obtained from the ZINC database) and the single crystal X-ray structure of DFP (**2**) were used without further preparation to investigate their binding modes and interactions within the binding pocket of SARS-Cov-2 S-RBD-ACE2 complex (PDB: 6M0J, Fig. 3) (Lan et al., 2020) and the active side in domain III from SARS-Cov-2 M^{pro} in complex with nirmatrelvir (PDB: 7VH8, Fig. 4) (Zhao, 2022). Following standard procedures (Tzvetkov et al., 2017), the binding modes and affinities were computed and visualized with the software SeeSAR (SeeSAR package version 12.1 Narcissus from BioSolveIT GmbH, St. Augustin, 2019) using HYDE algorithm as implemented in SeeSAR (see Experimental Section) (Schneider et al., 2013; Schärfer et al., 2013; Reulecke et al., 2008; Schneider et al., 2012). The implementation of the SCXRD/HYDE platform for structure-based drug design and virtual screening (Tzvetkov et al., 2017) suggests that both molecules are highly flexible and able to bind to hACE2 from the SARS-Cov-2 S-RBD-ACE2 complex (both DFP and FAV, Fig. 3) and to the active side in domain II of SARS-Cov-2 M^{pro} (preferred binding of DFP *vs.* FAV, Fig. 4). The most important interactions (hydrogen bond and hydrophobic contacts) of FAV and DFP within the binding pocket of both targets of interest are summarized in Table 1.

First, we evaluated the binding of FAV and DFP to hACE2 from the SARS-Cov-2 S-RBD-ACE2 complex (Fig. 3). The proposed binding modes and estimated affinities strongly indicate that both compounds occupy the same substrate cavity space forming two (for FAV) and one (for DFP) hydrogen bonds with residues Ile291/Asn290 and Ile291, respectively. This was expected because both compounds are planar small molecules, which are able to fit into and fill the lipophilic space of hACE2 formed mostly by Pro and Phe residues. The computed binding modes for FAV indicate the occurrence of a lactim-lactam tautomerism (Antonov, 2020) in which the lactam form seems to be more stable under physiological conditions and thus responsible for the formation of both H-bonds. Furthermore, we found that the conformation of FAV is additionally stabilized by the formation of an intramolecular bond within the carboxamide function (CO–––NH_2CO ≈ 1.79 Å), which plays an essential role for its conformation within the substrate cavity region of hACE2 (*cf.* Table 1). Compared to FAV (**1**), the computed binding mode of DFP (**2**) suggests that the only relevant H-bond is highly coordinated also by a higher number of hydrophobic interactions (ten for DFP *vs.* five for FAV). Three of these hydrophobic interations, i.e., with Ile291, Pro415, and Phe438 are common for both compounds (*cf.* Table 1). Moreover, the carbonyl groups of both compounds FAV and DFP serve as a hydrogen bonding domain (HBD) to form hydrophilic H-bond interactions, while the rest of the molecules represent the hydrophobic structural parts, e.g., the 6-fluoropyrazine and the 1-methylpyridin moiety in FAV and DFP, respectively. As a result, FAV and DFP occupy a strongly hydrophobic binding pocket dominated by hydrophobic contacts with isoleucine (Ile), leucine (Leu), proline (Pro), and phenyl residues.

Next, we investigated the binding modes of FAV and DFP to the active side in domain II of SARS-Cov-2 M^{pro}. The co-crystalized covalent bonded ligand PF0732133 (nirmatrelvir, Figure S3) was taken as a reference in order to investigate and validate the binding modes of FAV

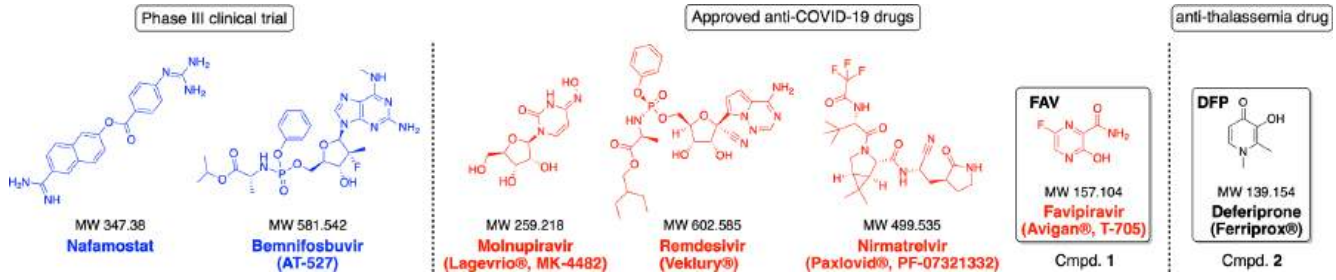

Fig. 1. Chemical structures and molecular weights of drug candidates in phase III clinical trial (in blue) and approved drugs (in red) as COVID-19 antivirals. The proposed herein drugs favipiravir (FAV, cmpd. **1**) and the anti-thalassemia drug deferiprone (DFP, cmpd. **2**) are highlighted. (For interpretation of the references to colour in this figure legend, the reader is referred to the web version of this article.)

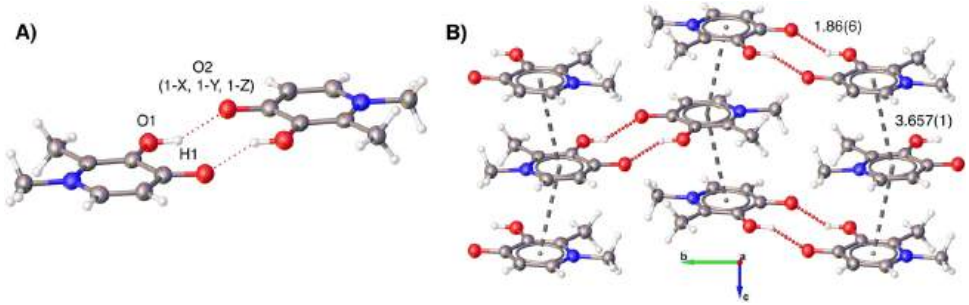

Fig. 2. A) Representation of the dimeric structure of DFP (**2**) obtained by single X-ray analysis. The formed H-bonds (O1–H1…O2) between the enolic groups of two molecules of **2** are indicated. B) The crystal packing of **2**, viewed from *a*-axis, showing a double layer along the *a*-axis. The π-π stacking and the formed H-bonds of the dimeric forms together with their distance are shown with bold red and grey dashed lines, respectively. (For interpretation of the references to colour in this figure legend, the reader is referred to the web version of this article.)

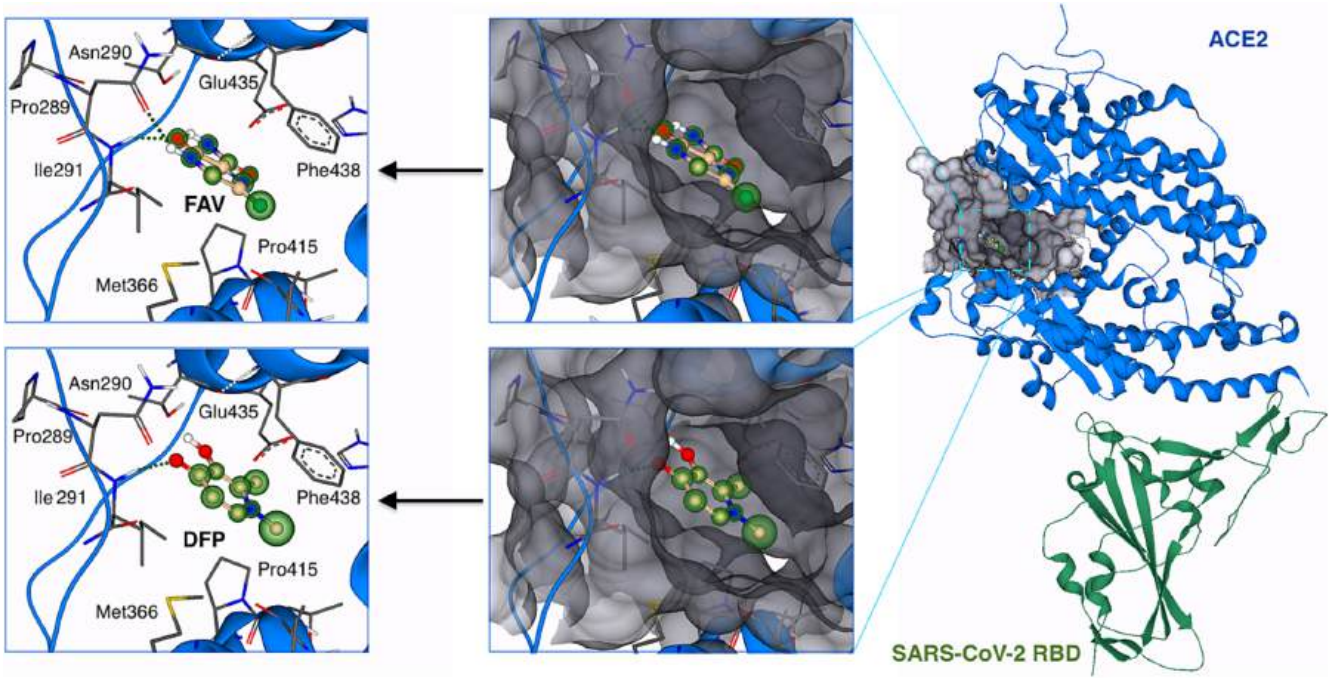

Fig. 3. Molecular docking experiments with favipiravir (FAV, 1) and deferiprone (DFP, 2) on SARS-Cov-2 S-RBD-ACE2 (PDB: 6M0J) using SeeSAR v.12.1 (SeeSAR package version 12.1 Narcissus from BioSolveIT GmbH, St. Augustin, 2019). The X-ray structure of the receptor-binding domain (RBD) of the spike protein (S-RBD, green ribbons) of SARS-Cov-2 is bound to the cell receptor ACE2 (blue ribbons) (Lan et al., 2020). The binding modes of 1 and 2 (HYDE colored ball-and-stick model) are shown in the active site of the hydrophobic pocket of ACE2 (middle part) together with the main H-interactions (left part). The binding residues are depicted in atom-colored stick model and the H-bonds are shown in green dotted lines, respectively. The HYDE corona coloring of the atomic affinity contributions: green = good, red = bad for binding affinity. (For interpretation of the references to colour in this figure legend, the reader is referred to the web version of this article.)

and DFP within the active site of SARS-Cov-2 M^{pro} (for DFP, see Figure S4). Analogously to the approved anti-COVID-19 drug nirmatrelvir, FAV and DFP occupy the same binding pocket in domain II, formed mainly by methionine (Met49 and 165), histidine (His41 and 164), and glutamine (Gln189) residues, as well as water molecules W592 and 594 (Table 1, Fig. 4 and S3). Both compounds show one hydrogen bond interaction with Gln189, while the peptidomimetic nirmatrelvir which is covalently bonded to Cys145 shows six H-bonds, three of which are with Glu166 (Figure S4).

Moreover, FAV and DFP form an equal number of hydrophobic interactions, the most important of which being with His41, His164, and Met49. The computations for the binding of FAV to of SARS-Cov-2 M^{pro} showed that the best docking pose represents its lactam tautomer confirming our observations for the active lactam form of FAV, in which the NH proton is crucial for hydrogen bond interactions and thus the ligand's stabilization within the binding site of SARS-Cov-2 hACE2 and M^{pro}. For simplification in the discussion below we will use the term 'keto-enol' tautomerism or keto and enol tautomers, respectively, for both FAV and DFP. These results are in agreement with our previous investigations, both theoretically and experimentally, that the keto form of FAV can be stabilized in proton acceptor solvents like water (Deneva et al., 2023; Antonov, 2020; Antonov, 2020). Based on molecular docking experiments, DFP did not show any tautomeric changes of its best docking poses in the active site of both SARS-Cov-2 hACE2 and M^{pro} proteins.

Thermodynamic profiling of favipiravir (1) and deferiprone (2)

In order to get deeper understanding behind the binding modes of FAV (**1**) and DFP (**2**) and to compute estimations of binding affinities (so called $K_{i\ HYDE}$ ranges) at both biological targets of interest, we applied HYDE scoring and visualization as embedded in SeeSAR (Schneider et al., 2013; Schärfer et al., 2013; Reulecke et al., 2008; Schneider et al., 2012). The HYDE scoring function enables us to access the overall

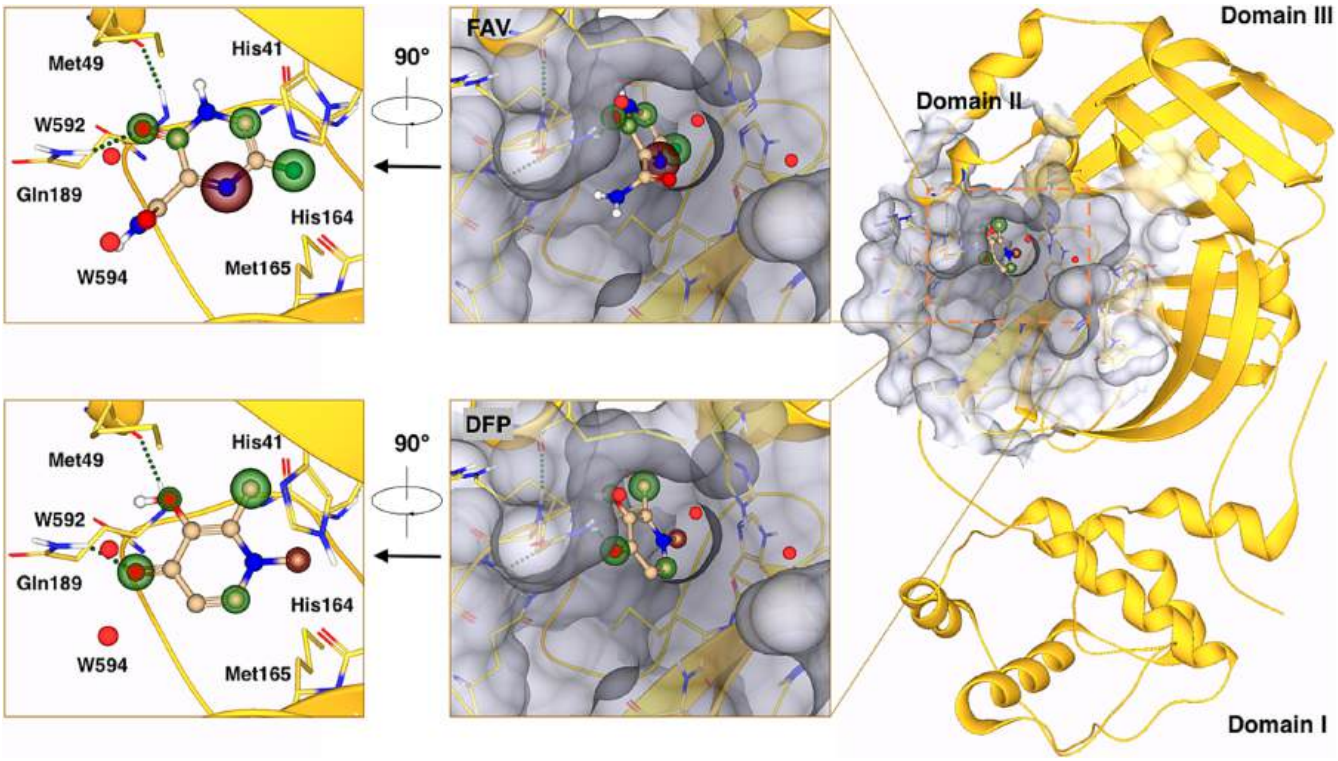

Fig. 4. Molecular docking experiments with favipiravir (FAV, 1) and deferiprone (DFP, 2) on SARS-Cov-2 main protease M^{pro} (BDB: 7VH8) using SeeSAR v.12.1 (SeeSAR package version 12.1 Narcissus from BioSolveIT GmbH, St. Augustin, 2019). The three domains (I–III) of SARS-CoV-2 M^{pro} (colored in goldenrod cartoon) are indicated (Zhao, 2022). The binding modes of 1 and 2 (HYDE colored ball-and-stick model) are shown in the active site of the hydrophobic pocket of M^{pro} domain II (middle part) together with the main H-interactions (left part, rotated at 90°). The binding residues are depicted in yellow stick model and the H-bonds are shown in green dotted lines, respectively. The water molecules W592 and W594 are indicated. The HYDE corona coloring of the atomic affinity contributions: green = good, red = bad for binding affinity. (For interpretation of the references to colour in this figure legend, the reader is referred to the web version of this article.)

Table 1
Binding interactions (hydrogen bond and hydrophobic interactions) of favipiravir (FAV) and deferiprone (DFP) within the binding pocket of SARS-Cov-2 ACE2 and M^{pro}. The most important residues are indicated in bold.

Compound	SARS-Cov-2 ACE2 (BDB: 6M0J)		SARS-Cov-2 M^{pro} (PDB: 7VH8)	
	Hydrogen bonds	Hydrophobic interactions	Hydrogen bonds	Hydrophobic interactions
FAV	Asn290 **Ile291** Intramolecular bond: C = O—NH_2CO (1.79 Å)	**Ile291**, Met366, Leu370, **Pro415**, **Phe438**	**Gln189**	**His41**, **Met49**, **His164**, Met165, Glu166, Asp187, Arg188, **Gln189**
DFP	**Ile291**	Pro289, Asn290, **Ile291**, Ala413, Thr414, **Pro415**, Thr434, Glu435, **Phe438**, His540	**Gln189**	**His41**, **Met49**, **His164**, Met165, Glu166, Asp187, Arg188, **Gln189**

binding thermodynamics of both compounds within the binding pocket of the respective target SARS-Cov-2 hACE2 and M^{pro}. HYDE considers the hydrogen bond (approximated as mainly enthalpic) and dehydration (approximated as mainly entropic) terms of the energy of binding (Gibbs free energy ΔG, kJ/mol) using a log*P*-based atomic increment system (*cf.* Experimental section) (Schneider et al., 2013; Schärfer et al., 2013; Reulecke et al., 2008; Schneider et al., 2012). The visualization of each non-hydrogen (heavy atom) as spheres (called "HYDE coronas") concerns both the protein (Rec) and the ligand (Lig) energy terms as well (for details, see Figure S5, Tables S2 and S3). The thermodynamic profiles, HYDE estimated binding affinities (ΔG values and $K_{i\ HYDE}$ ranges), and important drug-like values for the best docking poses of FAV and DFP within the binding pocket of the respective SARS-Cov-2 hACE2 and M^{pro} protein are listed in Fig. 5. Similar virtual screening approach with subsequent experimental confirmation of estimated binding affinities were successfully applied for the determination of dually active peptidomimetics (Kühl et al., 2023). Our HYDE assessment provides valuable information about the superior affinity of DFP versus FAV with respect to SARS-Cov-2 hACE2 and M^{pro}. HYDE analyses revealed overall favourable contributions of all heavy atoms to ΔG estimated and visualized in DFP, e.g., lower ΔG values for DFP than for FAV (*cf.* Tables S2 and S3). The thermodynamic profiles of DFP showed predominant enthalpic contribution (ΔH = –16.9 and –18.8 kJ/mol for SARS-Cov-2 ACE2 and M^{pro}, respectively) and less (–TΔS = –1.9 kJ/mol for SARS-Cov-2 ACE2) or non-favorable entropic terms (–TΔS = 8.2 kJ/mol for SARS-Cov-2 M^{pro}) to the total binding energy ΔG, ranking from –18.8 (for SARS-Cov-2 ACE2) to –10.6 kJ/mol (for SARS-Cov-2 M^{pro}) (*cf.* Fig. 5A, Tables S2 and S3). In contrast, the contribution of all non-hydrogen atoms to ΔG in FAV is –12.8 and –4.2 kJ/mol for binding to SARS-Cov-2 ACE2 and M^{pro}, respectively. The thermodynamic profile of FAV showed also preferable enthalpic contributions (ΔH = –34.9 and –18.8 kJ/mol for SARS-Cov-2 ACE2 and M^{pro}, respectively) like those estimated for DFP, however, much more unfavorable entropic terms (–TΔS = 22.1 and 14.6 kJ/mol for SARS-Cov-2 ACE2 and M^{pro}, respectively).

Based on the HYDE binding affinities (ΔG in kJ/mol) for FAV and DFP, we found that there is a very good agreement between ΔG and the predicted $K_{i\ HYDE}$ ranges (from mM to low μM) for each compound

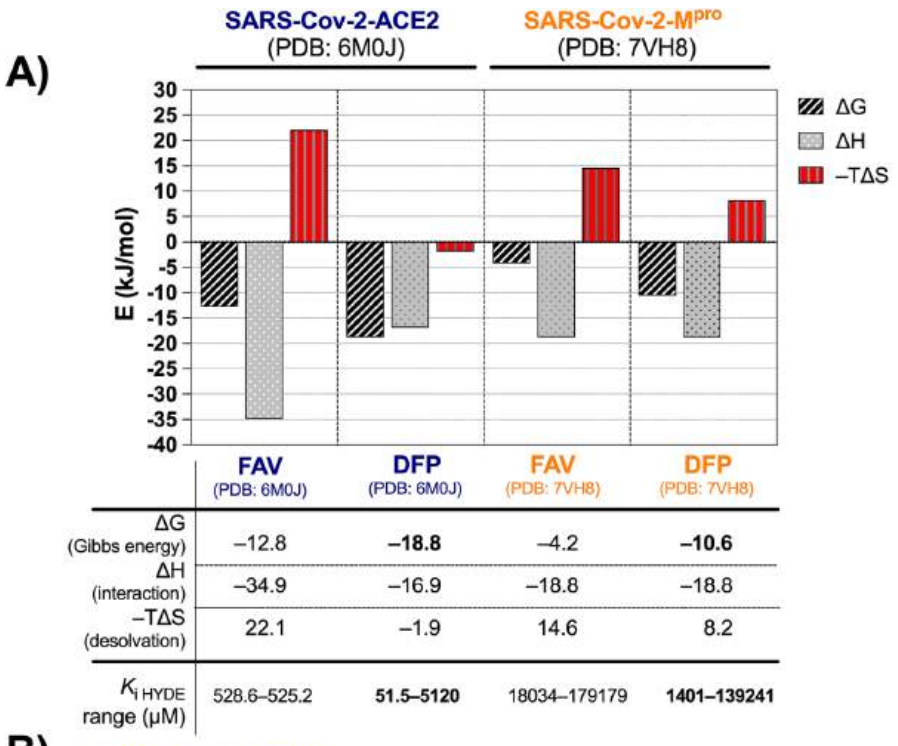

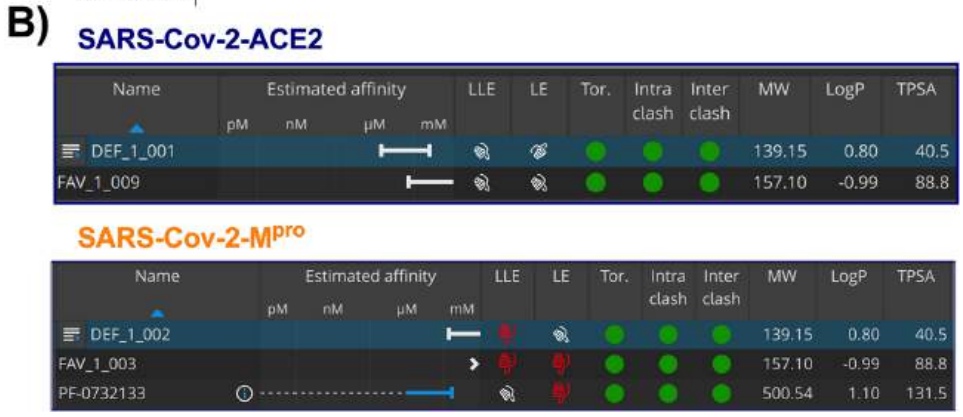

Fig. 5. A) Approximate computed thermodynamic profiling of FAV (1) and DFP (2) obtained from their best docking poses into SARS-Cov-2-ACE2 (PDB: 6M0J) and SARS-Cov-2-M^{pro} (PDB: 7VH8). The bar diagrams represent the semi-quantitative decomposition of enthalpic (ΔH: sum of interactions; in grey bars) and entropic part (–TΔS: sum of dehydration terms; in red) for all non-hydrogen/heavy atoms of the Gibbs free energy (ΔG = ΔH – TΔS, kJ/mol; in black). The estimated thermodynamic binding values (in kJ/mol) as well as binding affinities ($K_{i\ HYDE}$ ranges) for each ligand are summarized in the respective tables below the diagrams. B) Tabular representation of HYDE estimated affinity ranges (from mM to μM), the lipophilic ligand efficiencies (LLE), the ligand efficiencies (LE), the torsions (Tor.), the graphical intra-/intermolecular clash, and some important physicochemical characteristics for 1 and 2 as virtually screened against both X-ray structures. HYDE coloring scheme: green = good, orange/grey = less favorable, red = bad for affinity. Note that the "Estimated Affinity" tabulator displays logarithmic scaling, i.e., the first third per range column responds to 1…10 pM/nM, the second 10…100, and the third one to 100…1000 units. LLE and LE values are favorable (grey thumbs: + or 0), better (green thumbs: ++) or not favorable (red thumbs: –). Torsion "Tor." entries: sometimes observed (orange points) or rarely/not observed (red points), pointing to likely low-energy torsions in the ligand conformations. Intra- (ligand) and inter- (ligand-receptor) molecular clashes are not observed (green dots) or not important (orange dots) for the respective ligand-receptor interaction. HYDE scoring and calculation of the enthalpic and entropic terms have been computed with docked ligands into both X-ray structures using SeeSAR (SeeSAR package version 12.1 Narcissus from BioSolveIT GmbH, St. Augustin, 2019). (For interpretation of the references to colour in this figure legend, the reader is referred to the web version of this article.)

versus SARS-Cov-2 ACE2 and M^{pro} proteins (Fig. 5A). For example, DFP was predicted to show higher (more favorable) thermodynamic binding affinities (ΔG = –18.8 and –10.6 kJ/mol) than compound FAV (ΔG = –12.8 and –4.2 kJ/mol) against SARS-Cov-2 ACE2 and M^{pro}, respectively. For comparison, the HYDE estimated lowest boundaries of the $K_{i\ HYDE}$ ranges for DFP were found to be almost 10- and 13-fold smaller than for FAV (51.5 μM *vs.* 529 mM at SARS-Cov-2 ACE2; 1401 *vs.* 18034 mM at SARS-Cov-2 M^{pro}). This suggests a much-preferred binding of DFP *vs.* the ones of FAV against both targets. A HYDE visual assessment of binding and torsional analysis of the best ranked docking poses for FAV and DFP in the active site of SARS-Cov-2 ACE2 and M^{pro}, respectively, indicates a good thermodynamic stabilization for both compounds via formation of keto tautomer and one intramolecular hydrogen bond (for FAV) and stable enol form (for DFP). Furthermore, SeeSAR's traffic light coloring scheme for torsions (Tor) and clashes (intra- and intermolecular) in FAV and DFP suggested an optimal ligand conformation within both proteins (favorable "*green*" torsions and clashes) (*cf.* Fig. 5B). The scheme is based on crystal structure statistics (Schneider et al., 2013; Schärfer et al., 2013; Reulecke et al., 2008; Schneider et al., 2012).

We should note that we have good reasons to believe in the accuracy of the docking studies and the subsequent HYDE analyses: (i) both compounds exhibit similar poses within the binding pocket of SARS-

Cov-2 ACE2, (ii) both compounds occupy exactly the same binding region as observed for the covalently bonded anti-COVID-19 drug nirmatrelvir in the co-crystal structure 7VH8, (iii) the trends of binding affinities ΔG (in kJ/mol) and predicted $K_{i\ HYDE}$ ranges (from mM to low μM) are correctly reproduced, and (iv) the computations are in line with experimentally confirmed keto tautomer formation of FAV in the presence of water (Schneider et al., 2013; Schärfer et al., 2013; Reulecke et al., 2008; Schneider et al., 2012).

Design of novel antivirals based on favipiravir (1) and deferiprone (2)

Based on the obtained docking models for FAV (**1**) and DFP (**2**) in both targets of interest SARS-Cov-2-ACE2 and M^{pro}, we further performed tautomer-based drug design in order to generate ideas for new antivirals using the same 3D protein structures as described above. Looking at the most stable tautomeric forms from the docking studies, the keto form for **1** and the unchanged most stable enol form for **2**, it can be concluded that both compounds possess a certain potential for further structural optimization in regards to improvement of biological activity towards both target proteins, for example via introduction of one or more lipophilic substituent. Starting from the best docking poses for both compounds, respectively, a set of structural analogs was designed and virtually screened against the active sites of SARS-Cov-2-ACE2 and SARS-Cov-2-M^{pro} (Table 2, Figure S5). According to our results, modifications via introduction of one or two lipophilic substituents at the carboxamide function and/or at position 2 in the structure of FAV (*cf.* Table 2, structures **1a–1c**) led to an increase of estimated $K_{i\ HYDE}$ values (from high to low μM values) for both targets. For DFP, such modifications can be introduced at positions 5 and/or 6 as well as via substitution of the methyl group at position 3 by a hydroxyethyl substituent (*cf.* Table 2, structures **2a–2c**). Overall, the compounds seem to be more selective towards SARS-Cov-2-hACE2 than to SARS-Cov-2-hM^{pro}, being virtually more active against SARS-Cov-2-hACE2 by about a factor of 353 (for **1b**) and > 48 (for **2b**), respectively, when compared with their parent compounds FAV (**1**) and DFP (**2**). However, in regards to dual activity, modifications in the parent structure of DFP seem to be significantly better tolerated than those in FAV. Considering the virtual activity against both target proteins, the most successful (virtual) modifications in the series of FAV appear to be those in compound **1c**, while the DFP derivative **2b** showed > 48- and about 12-fold increase in virtual activity towards both biological targets. The results from virtual screening towards SARS-Cov-2-ACE2 and M^{pro} using the best docking poses of FAV and DFP suggests both compounds to be promising model drugs for performing a tautomer-based drug design of novel small-molecule antivirals against SARS-Cov-2.

Tautomerism of favipiravir (1) and deferiprone (2)

In order to get more detailed information about the possible tautomer formation, FAV (**1**) and DFP (**2**) were further analyzed for their tautomerism by means of quantum-chemical calculations at the M06-2X/TZVP level of theory. For simplification in the discussion for **1**, enol and keto terms are used instead of lactim–lactam tautomerism. The structures of the most stable 'keto-enol' tautomers for compounds **1** (**1E** and **1K**) and **2** (**2E**, **2K** and **2CH**) used for further investigations are shown in Fig. 6. In the case of favipiravir (**1**), the rotation of the carboxamide and the hydroxyl groups offers additional possibilities for each of the tautomers (**1E** and **1K**) to form isomers, e.g., isomers **1E'**, **1E''** for the enol form **1E** and the only **1K'** isomer for the keto form **1K** (*cf.* Fig. 6). Among all these possible isomers, **1E** and **1K** represent the most stable 'keto-enol' forms due to their stabilization via an intramolecular hydrogen bonding depending on the orientation of the OH group (for **1E**) and the amide group (for **1K**) (Deneva et al., 2023). Deferiprone (**2**) can potentially exist as three tautomeric forms – enol **2E**, keto **2K** and *di*-keto **2CH** form (*cf.* Fig. 6). Two of them, the enol form **2E** and the zwitterion form **2K**, are stabilized via an intramolecular

Table 2
Selected hits with their chemical structures (incl. SMILES), estimated binding affinity (the lowest predicted $K_{i\ HYDE}$ values and ranges μM) within the binding pocket of SARS-Cov-2 ACE2 and M^{pro}. Compounds are derived from FAV (**1**) and DFP (**2**) and selected according to their computed $K_{i\ HYDE}$ values. The lowest $K_{i\ HYDE}$ values for both compounds against each biological target are indicated.

Compound	$K_{i\ HYDE}$ lowest predicted values (ranges) (μM)	
	SARS-Cov-2 ACE2 (BDB: 6M0J)	SARS-Cov-2 M^{pro} (PDB: 7VH8)
 **1 (FAV)**	529 (529–52,516)	1,803 (1,803–1,791,788)
NC(C1 = NC(F) = CNC1 = O) = O		
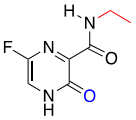 **1a**	7.61 (7.61–756)	n.a.
CCNC(C1 = NC(F) = CNC1 = O) = O		
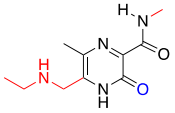 **1b**	**1.50** (1.50–149)	3,254 (3,254–323,297)
CC[NH2 +]CC(N1) = C(C)N = C(C(NC) = O)C1 = O		
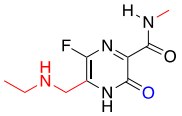 **1c**	**5.89** (5.89–585)	**835** (835–82,936)
CC[NH2 +]CC(NC(C(C(NC) = O) = N1) = O) = C1F		
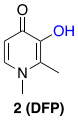 **2 (DFP)**	51.5 (51.5–5,120)	1,401 (1,401–139,241)
CC(N(C)C = CC1 = O) = C1O		
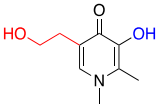 **2a**	3.80 (3.80–338)	299 (299–29,745)
CC(N(C)C = C(CCO)C1 = O) = C1O		
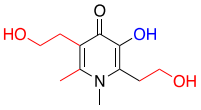 **2b**	**1.07** (1.07–106)	**118** (118–11,746)
CC(N(C)C(CCO) = C1O) = C(CCO)C1 = O		
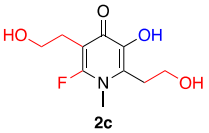 **2c**	3.36 (3.36–334)	265 (265–26,355)
CN(C(CCO) = C1O)C(F) = C(CCO)C1 = O		

n.a. = not active.

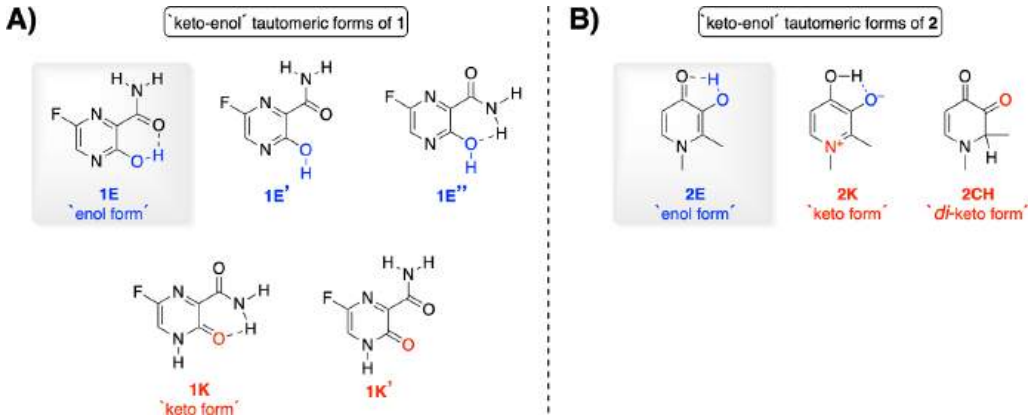

Fig. 6. Possible tautomeric (**1E** and **1K**) and isomeric forms (**1E', 1E''** and **1K'**) of **1** (A) and most stable possible tautomers of **2** (B). The indication **E** corresponds to the enol forms, while **K** corresponds to the keto tautomers.

hydrogen bond formation between keto and hydroxyl groups making these isomers more stable in comparison with the *di*-keto **2CH** tautomer, which can theoretically be formed by a transfer of a hydrogen atom of the α-hydroxyl group in the neighbor β-position.

Therefore, the theoretical calculations were performed with the most stable tautomers **1E** and **1K** (for FAV, **1**) and all three tautomeric forms **2E**, **2K** and **2CH** (for DFP, **2**) using the M06-2X/TZVP level of theory under considering the influence of different solvents. The optimized structures of these tautomers together with theoretically predicted relative stabilities in acetonitrile, DMSO, and water are summarized in Table 3. The theoretical results show very clearly that in solution favipiravir (**1**) and deferiprone (**2**) exist predominantly in their enol forms **1E** and **2E**, which are significantly more stable than the corresponding keto forms **1K** (for **1**) and **2K**/**2CH** (for **2**), respectively. It can be seen that the effect of the solvent polarity is negligible suggesting that under the used theoretical conditions, e.g., considering the solvent as a continuum, there is no tautomeric equilibrium for all investigated tautomeric forms. The calculated keto-enol relative energies (ΔE, kcal/mol) for the most energetically favorable tautomers showed almost equal differences between the enol (**1E** and **2E**) and the keto forms (**1K** and **2K**) in all solvents (*cf.* Table 3 and Figure S7). For compound **1**, there is 5.8 kcal/mol (in acetonitrile and DMSO) and 5.7 kcal/mol (in water) difference between the respective enol form **1E** and the keto form **1K**, while in an equal ΔE of 5.6 kcal/mol between the most stable enol form **2E** and the keto form **2K** was estimated (see Figure S7).

Photophysical evaluation of favipiravir (1) and deferiprone (2)

In the course of our comparative investigations, we performed further solvent-dependent photophysical experiments in order (i) to validate the accuracy of the molecular docking studies and virtual screening, obtained for the most likely docking poses for FAV (**1**) and DFP (**2**) within the active site of SARS-Cov-2-ACE2 and SARS-Cov-2-M^{pro}, (ii) to determine the biologically active tautomeric forms for FAV and DFP in the light of tautomeric-based drug design, i.e., with respect to new designed derivatives **1a–1c** and **2a–2c**, and (iii) to investigate the ability of DFP to form complexes with bivalent metal ions.

Electronic absorption spectra of FAV and DFP were measured in different solvents and water–solvent mixtures (Table 4, Fig. 7 and S8) and in the presence of Mg^{2+} ions (Fig. 8). In addition to the UV–VIS experiments, theoretical simulations to predict the absorption spectra in different solvents (e.g., DMSO, ACN and water) were performed and data compared with those observed from the experiments (see Supporting information, Figure S9). The absorption maxima (λ_{max}) of FAV were found to be 321 (in ACN) and 326 nm (in toluene) without remarkable spectral changes in the shape, while in an ACN–water solution (80 % water) a new broadband at 364 nm in addition to the λ_{max} at 323 nm can be observed (*cf.* Table 4, Fig. 7A). Moreover, the intensity of the band at 323 nm significantly decreases (Fig. 7A). The UV–VIS spectra of FAV confirmed the data from the quantum-chemical calculations suggesting that in polar aprotic solvents (e.g., ACN and toluene) FAV exists in its more stable enol form (**1E**), while in the presence of water the tautomeric equilibrium shifts towards the formation of its keto tautomer **1K** as a consequence of specific solute–solvent interactions (Deneva et al., 2023). In contrast, the absorption spectra of DFP (**2**) do not show any significant changes neither in different solvents (e.g., DMSO, ACN or methanol) nor in the presence of water (50 %). Compared to FAV, DFP exhibits lower λ_{max} values of 286 (in DMSO) and 283 nm (in ACN and MeOH) due to its pyridine moiety (Table 4). The addition of water to the respective solvent did not lead to a change in the absorption maxima, which was found to be almost equal ($\lambda_{max} \sim 282$ in DMSO–water, 50 % and $\lambda_{max} \sim 280$ in MeOH–water mixture). The results from the UV–VIS experiments for DFP are in line with those observed from the quantum-chemical calculations, revealing the existence of the only stable enol tautomer **2E** in different solvent solutions. The lack of solvent influence on the tautomerism of DFP is seen from the absorption spectra, showing identical band positions and almost identical molar absorptivities in pure solvents and water mixtures (including buffers at pH 7.4), which is one more evidence for the lack of tautomeric mixture (Fig. 7B and S8). Furthermore, both compounds FAV and DFP showed notable differences in their molar absorptivity (ε) measured in the appropriate solvents. The molar absorptivities observed for FAV are in general much higher than those measured for DFP and, for both compounds, decrease with increasing the solvent polarity. As expected, the lowest ε values were observed for FAV and DFP in solvent–water mixtures (Table 4).

In addition to the experimental results, we performed theoretical simulations of the UV–VIS spectra for the most stable tautomers of FAV (**1E** and **1K**) and DFP (**2E**, **2K** and **2CH**) in different solvents by using the B3LYP/TZVP level of theory as used for the optimized ground-state geometries (Kawauchi et al., 2014; Becke, 1993). The predicted spectra of keto-enol tautomeric forms for FAV (FAV-**1E** and FAV-**1K**) and DFP (DFP-**2E** and DFP-**2K**) in comparison with the measured absorption spectra for FAV and DFP in acetonitrile are shown in Fig. 8. It should be mentioned, that all spectroscopic experiments were performed at the same concentration for each compound (e.g., for FAV at 15 μM, for DFP at 30 μM) in order to measure solvent-dependent effects of both compounds. The obtained differences in the spectral intensity (and shape) are related to the different molar absorptivity of FAV and DFP in the specific solvent. The predicted spectra for the most stable tautomers of FAV and DFP in different solvents are shown in Figure S9 and the data collected in Tables S4–S6 (see Supporting information).

Independent of the modeled environment (e.g., DMSO, ACN or water), there are no essential differences between the simulated band

Table 3
Theoretically predicted relative stability (ΔE, ΔE + ZPE and ΔG, kcal/mol) of all possible tautomeric forms of favipiravir (FAV) and deferiprone (DFP) in various solvents at M06-2X/TZVP level of theory.

Tautomer	Structure (dipole moment in D)	acetonitrile			DMSO			water		
		ΔE	ΔG	ΔE + ZPE	ΔE	ΔG	ΔE + ZPE	ΔE	ΔG	ΔE + ZPE
FAV-1E	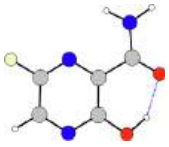 4.5	0.00	0.00	0.00	0.00	0.00	0.00	0.00	0.00	0.00
FAV-1K	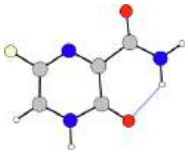 8.5	5.8	6.2	5.9	5.8	6.1	5.8	5.7	6.0	5.7
DFP-2E	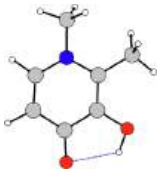 10.0	0.00	0.00	0.00	0.00	0.00	0.00	0.00	0.00	0.00
DFP-2K	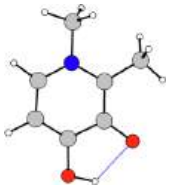 9.9	5.6	5.6	5.7	5.6	5.6	5.7	5.6	5.6	5.7
DFP-2CH	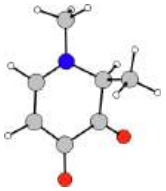 11.7	18.1	17.9	17.2	18.1	17.9	17.2	18.0	17.8	17.1

positions as shape as well as the theoretically predicted long-wavelength absorption maxima (λ_{max}) and the oscillator strengths (*f*) at the $S_0 \rightarrow S_1$ transition state for each tautomer of FAV and DFP (Figure S9, Tables S4–S6). This is not surprising having in mind that according to the experimental UV–VIS studies the type of the solvent employed, affect the significant predominance of the enol forms **1E** and **2E** in polar aprotic solvents, while in the presence of water the keto form **1K** of FAV can be observed (*cf.* Fig. 7A). According to the theoretical simulations and independent of the type of solvent, the keto form **1K** of FAV should be accompanied by a red shift in the spectra with calculated λ_{max} of ~ 338–339 nm, which can be experimentally observed for FAV only in the presence of water where an additional absorption band at 364 nm appeared (*cf.* Fig. 7A and Table 4). Moreover, the predicted spectra in all solvents for the keto form **1K** of FAV showed different shape (bands at ~ 338–339 and 290 nm), compared with the simulated bands of the enol form **1E** (Fig. 8A and S9). In polar aprotic solvents, the calculated

Table 4
Photophysical data of FAV **1** (15 μM) and DFP **2** (30 μM) in different solvents.

FAV						DFP									
ACN		Toluene		ACN–H_2O (20:80 %)		DMSO		DMSO–H_2O (50 %)		ACN		MeOH		MeOH–H_2O (50 %)	
λ_{max} [a]	ε [b]	λ_{max}	ε	λ_{max}	ε	λ_{max}	ε	λ_{max}	ε	λ_{max}	ε	λ_{max}	ε	λ_{max}	ε
321	6914	326	5886	323 364	4337 2752	286	1697	282	1436	283	1658	283	1688	280	1461

[a] Unit: nm. [b] Unit: $M^{-1}cm^{-1}$.

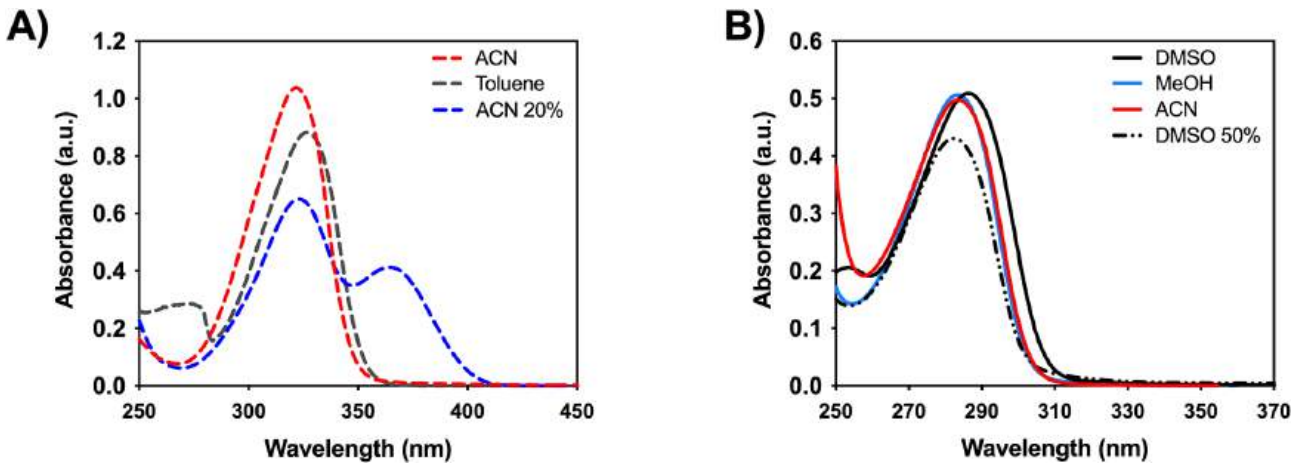

Fig. 7. A) Absorption spectra of FAV (15 μM) in ACN, toluene, and 50 % ACN (Deneva et al., 2023). B) UV–VISible absorption spectra of DFP (30 μM) in DMSO, methanol (MeOH), acetonitrile (ACN), and 50 % DMSO.

spectra revealed that FAV exists in its enol form **1E**, which is in agreement with the results obtained for FAV from the experiments.

The same is seen for DFP (see Fig. 8B and S9, Tables S4–S6). The theoretical calculations predict no solvent effect for each tautomer of DFP, however, with differences in the position of the long-wavelength absorption band with λ_{max} at 258 (**2E**), ~312 (**2K**) and ~ 428 (**2CH**) nm in all used solvents at the $S_0 \rightarrow S_1$ transition state, which confirms the experimental observations for the most stable enol form **2E** of DFP. In the case of FAV, the increase of the solvent polarity leads to a reduction of the relative energy, i.e., the more polar keto tautomer **1K** is stabilized, but insufficiently. This effect is not observed in the case of DFP, where the tautomers are equally polar. In both compounds the proton transfer is energy demanding, because it happens either through rotational rearrangement (as in favipiravir) or through 5-membered cyclic hydrogen bonding. In the case of irradiation of favipiravir, a phototautomer is obtained, which does not relax to the ground state keto form **1K**, restoring the enol **1E** (Figure S9). In the case of deferiprone, it is highly possible that the ESIPT process can lead to excited keto tautomer **2K**, which, by relaxing back to the ground state should restore the enol form **1E** through GSIPT. The lack of keto tautomerism for DFP is due to the fact that in the most stable enol tautomeric form is no proton acceptor and proton donor sites that are available for interaction with the water molecules. It should be mentioned that the best docking solutions within the active site of SARS-Cov-2-ACE2 and SARS-Cov-2-M^{pro}, including the virtually designed new structures **1a–1c** and **2a–2c**, showed the existence of keto forms for FAV and DFP under physiological conditions, i.e., in the presence of water. Moreover, the herein obtained theoretical results for FAV are in agreement with recently performed experimental studies, showing that in aqueous solutions the tautomeric equilibrium is shifted towards the keto tautomer **1K** due to the stabilization of the keto form via formation of water–FAV clusters, while in solvents like ACN or toluene the enol form **1E** seems to be preferable (Deneva et al., 2023).

In addition to the experimental and theoretical studies, the ability of FAV and DFP to form complexes in ACN with Mg^{2+} was investigated to compare their chelating activity in the context of their affinity towards both targets SARS-Cov-2-ACE2 and SARS-Cov-2-M^{pro} and, thus, to examine their additional potential therapeutic effects as antiviral drugs. Together with other essential metal ions, such as iron, copper, zinc, cobalt, or selenium, bivalent manganese (Mg^{2+}) plays an important role in maintaining the intracellular processes in humans (Kontoghiorghes and Kontoghiorghe, 2020). It is well-known that DFP is a strong bidentate chelating agent of Fe^{3+} and is selective for tribasic metal cations (Kontoghiorghes and Kontoghiorghe, 2020; Cilibrizzi et al., 2018). Therefore, in this study we explored the chelating activity of DFP towards Mg^{2+} in comparison with those of FAV. The complexations experiments were performed by using UV–VIS spectroscopy in ACN as a solvent and the spectral changes upon addition of $Mg(ClO_4)_2$ (for FAV) or $MgCl_2$ (for DFP) were recorded (Fig. 9). As recently discovered, FAV showed selective ability to form complexes with bivalent metal ions like Mg^{2+} and Ca^{2+} with logarithmic stability constants of 1.13 ± 0.04 and 0.75 ± 0.05 for the 2:1 ligand:metal complexes of Mg^{2+} and Ca^{2+},

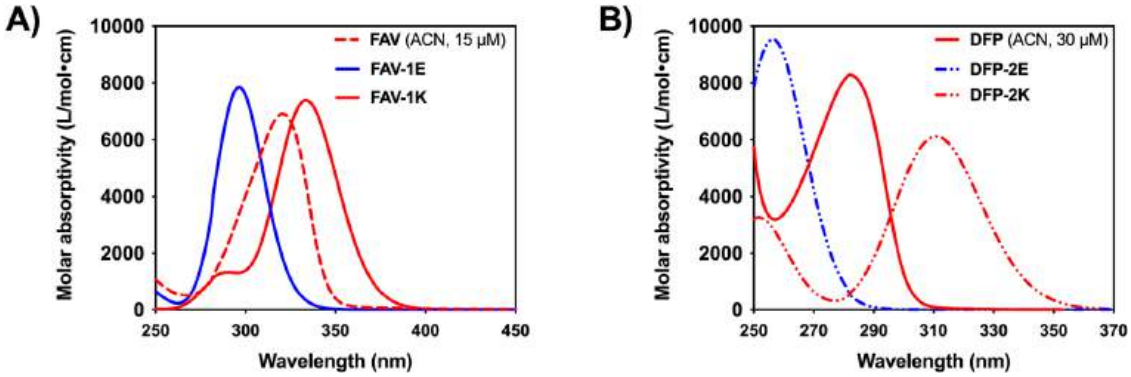

Fig. 8. A) Comparison between the experimental and the simulated absorption spectra (B3LYP) in ACN for FAV (15 μM, red dashed line) and enol (FAV-**1E**, blue solid line) and keto form (FAV-**1K**, red solid line). B) Comparison between the experimental and the simulated absorption spectra (B3LYP) in ACN for DFP (30 μM, red solid line) and the pure enol (DFP-**2E**, blue dash-dotted line) and keto form (DFP-**2K**, red dash-dotted line). (For interpretation of the references to colour in this figure legend, the reader is referred to the web version of this article.)

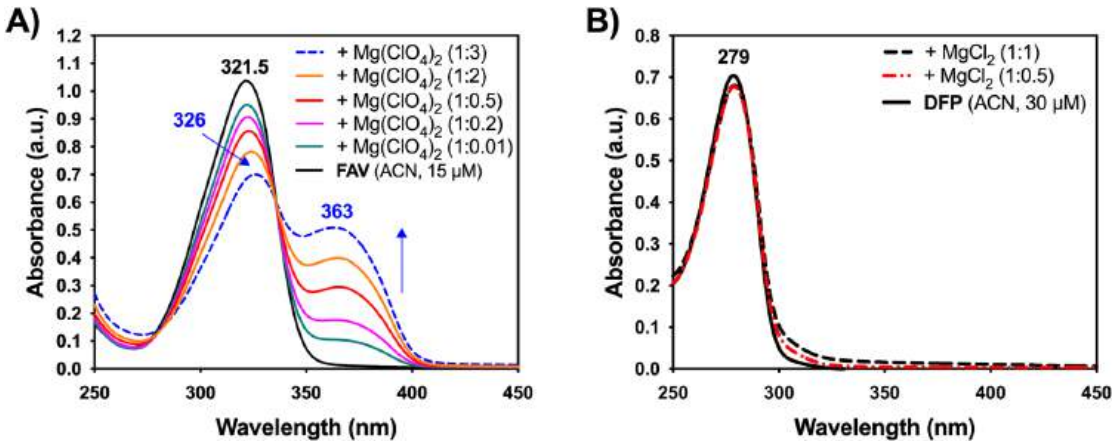

Fig. 9. A) UV–visible absorption spectra of FAV 1 (15 μM, black solid line) in ACN with different molar ratios of $Mg(ClO_4)_2$. The absorption maxima of pure FAV (1) and its complex with $Mg(ClO_4)_2$ is indicated (Deneva et al., 2023). B) Absorption spectra of DFP 2 (30 μM) in ACN (black solid line) with different molar ratios of $MgCl_2$ (dashed lines).

respectively (Deneva et al., 2023). As seen in Fig. 9A, the addition of water to the solution of FAV in ACN lead to the appearance of a new spectral band at 363 nm, while the absorption maxima at ~ 323 nm decreases with increasing the concentration of Mg^{2+} in the solution. The observed spectral changes indicated the formation of a $(FAV)_2$–Mg complex occurring after deprotonation of FAV in solution, which is confirmed by ESI-HRMS and ^{19}F NMR studies (Deneva et al., 2023). In the case of DFP, the addition of $MgCl_2$ did not cause any spectral changes (Fig. 9B).

Since DFP is widely used standard as a Fe^{3+} chelating agent against iron overload, further metal-binding experiments were performed with DFP upon addition of $FeCl_3$ or $FeSO_4$ in DMSO (50 %) (Habib et al., 2021). The experiments were performed by a stepwise titration of an isomolar solution of DFP (30 μM in 50 % DMSO) with an equal amount (10 μL) of the respective solid solution in DMSO. The UV–VIS spectra were recorded after each addition of the respective solid by using the same experimental conditions as used for the UV–VIS spectroscopic experiments (e.g., at room temperature and device settings). The measured UV–VIS spectra are shown in Figure S10 (see Supporting information). Therefore, the logarithmic stability constants (logβ) of the 3:1 and 2:1 DFP–iron complexes of Fe^{3+} and Fe^{2+} were calculated to be 35.9 ± 0.4 and 14.7 ± 0.08, respectively. These values are in agreement with the literature data for DFP binding to iron in a 3:1 ratio with estimated logβ values of 35.0 (Kontoghiorghes and Kontoghiorghe, 2020) and 37.2 (Cilibrizzi et al., 2018).

The data obtained from chelate binding studies suggested that FAV is able to form stable complexes with bivalent alkali-earth-metal ions (Mg^{2+} or Ca^{2+}) depending on the stabilization energies of the respective ligand–metal complex (Deneva et al., 2023), while DFP shows > 2.5-fold higher affinity towards tribasic than against dibasic metal cations. Nevertheless, DFP exhibit stronger metal chelating properties than FAV due to its more stable enol tautomeric form ensuring easy deprotonation of the α-hydroxyl group and, thus, stabilization of the formed DFP–metal complexes.

Biological studies and in silico evaluation of favipiravir (1) and deferiprone (2)

In the context of tautomer–based drug design of novel antivirals with improved safety profile, simultaneously affecting SARS-Cov-2-ACE2 and SARS-Cov-2-M^{pro} targets of interest, we further performed *in vitro* study of relevant physicochemical and toxicity (ADME-T) parameters of FAV and DFP. The obtained results from the different *in vitro* assays including some estimated pharmacological values are summarized in Table 5.

As mentioned above, the antiviral drug favipiravir (FAV, also known as T-705) is used against influenza viruses and approved for emergency use in many countries as an effective alternative for COVID-19 treatment (Gunaydin-Alkyildiz et al., 2022). It is well-known that FAV is used as a prodrug, which is phosphoribosylated by cellular enzymes to its metabolite favipiravir-ribofuranosyl-5′-triphosphosphate (FAV-RTP) (Gunaydin-Alkyildiz et al., 2022; Jin et al., 2013), providing additional information regarding its *in vivo* active tautomeric form **2K**. This predetermined the function of the biologically active FAV tautomer **2K** as a purine analog with higher affinity (IC_{50} = 341 nM) towards viral RNA-dependent RNA polymerase (RdRp) than to guanosine triphosphate (GTP) (Gunaydin-Alkyildiz et al., 2022; Jin et al., 2013; Futura et al., 2013). Therefore, FAV is under wide investigations for its side effects, many of them related to the gastrointestinal system (Gunaydin-Alkyildiz et al., 2022). However, recent studies suggest that FAV could also inhibit CYP2C8 with an IC_{50} of 477 μM (74.9 μg/mL) (Michaud et al., 2021), but also cause cardiotoxicity, which is associated with the effects of FAV on the human ether-a-go-go-related gene (hERG) at a concentration of 1.0

Table 5
In vitro and *in silico* ADME-Tox parameters of favipiravir (FAV, **1**) and deferiprone (DFP, **2**).

	FAV	DFP
Cytotoxicity assay (% of control ± SD @100 μM)		
MDA-MB-231 viability (24 h / 72 h)	106 ± 5.5 / 99.9 ± 10.6	102 ± 0.6 / 110 ± 5.2
HepG2 viability (24 h / 72 h)	110 ± 5.0 / 96.2 ± 7.6	99.8 ± 0.6 / 100 ± 1.3
3 T3 viability (24 h / 72 h)	107 ± 6.3 / 85.6 ± 6.9	98.4 ± 6.6 / 100 ± 4.2
CYP inhibition (@50 μM)[a)]		
CYP1A2	No inhibition	No inhibition
CYP2C9	No inhibition	No inhibition
CYP2C19	No inhibition	No inhibition
CYP2D6	No inhibition	No inhibition
CYP3A4	No inhibition	No inhibition
Aqueous solubility (mg/mL, @pH 7.4)	< 1.0 (@25 °C)	≥ 11.0 (@37 °C)
CLog$D_{7.4}$[a)]	–1.72	–0.45
CLog$P$[a)]	0.62	–0.47
tPSA ($Å^2$)[a),b)]	89.10	40.54
PAMPA-BBB permeability (±SD, n = 3)		
P_e (×10^{-6} cm/s), donor pH 7.4 / acceptor pH 7.4	<0.01	0.29 ± 0.02
–logP_e	>8.0	6.53 ± 0.04

[a)]Predicted values using ACD/Percepta software tool v. 14.0.0 (https://www.acdlabs.com). [b)] tPSA = topological polar surface area. n.d. = not determined.

mM (Gunaydin-Alkyildiz et al., 2022; Michaud et al., 2021). Thus, the suppression of hERG is linked with a high risk for drug-induced cardiac repolarization (QTc prolongation), also known as long QT syndrome (LQTS). Therefore, close monitoring of the QTc interval during the treatment of COVID-19 patients remains advisable (Gunaydin-Alkyildiz et al., 2022; Michaud et al., 2021; Esmel-Vilomara, 2022). Due to the quite high effective doses of FAV (2 × 1600 mg loading dose on the first day followed by 2 × 600 mg, $C_{max} = 328$ μM and $t_{1/2} = 2$–5.5 h), several adverse effects during and after patient's treatment with FAV can be expected especially at the molecular level (Gunaydin-Alkyildiz et al., 2022). For example, recent cytotoxic studies with H9c2 cardiomyoblasts and CCD-1079Sk skin fibroblasts have shown that FAV can cause genotoxic and oxidative stress-inducing DNA damage at a concentration of 400 μM (Gunaydin-Alkyildiz et al., 2022). In contrast to FAV, there are less adverse effects of DFP occurring during the treatment of iron overload (Entezari, 2022). However, the significant side effects of DFP are agranulocytosis and neutropenia, while gastrointestinal symptoms, arthropathy, musculoskeletal pains, zinc deficiency, and some others are less frequent severe events that occur after a long-term therapy with DFP (Entezari, 2022). Nevertheless, DFP is considered as the best chelating agent in reducing cardiac iron overload, especially when used in combination with other chelators such as deferasirox (Entezari, 2022).

Therefore, we further investigated the cytotoxic effects of FAV and DFP in order to examine the potential drug-induced cytotoxicity in human breast adenocarcinoma MDA-MB-231, hepatocarcinoma HepG2, and mouse embryonic fibroblasts 3T3 cells. The cytotoxicity experiments were performed according to our previously described protocols using MTT assay (Kühl et al., 2023; Tzvetkov et al., 2019). The cell viability was initially determined after a 24 and 72 h incubation period in a concentration range of 0.1–100 μM that is usually applied in the drug development. As seen in Fig. 10, in the tested low concentration range, the cytotoxicity profile of FAV and DFP followed the same trend in all three cell lines as observed for the untreated control groups. For both compounds, no pronounced effects on cellular viability were detected neither after 24 nor 72 h incubation (Fig. 10, Table 5). Compared to the untreated control, the cell viability ranges between ~ 86 % (for FAV at 72 h, 3T3 cells) and 110 % (for Fav at 24 h, HepG2; for DFP at 72 h, MDA-MB-231 cells), indicating that both FAV and DFP did not show any cytotoxic effect on MDA-MB-231, HepG2 and 3T3 cells within the tested low concentration range (Table 5).

Since the cytotoxic studies with H9c2 cardiomyoblasts and CCD-1079Sk skin fibroblasts have shown that FAV can cause DNA damage at a high concentration of 400 μM (Gunaydin-Alkyildiz et al., 2022), we performed additional cytotoxic studies with FAV and DFP in higher concentrations up to 1000 μM. The cytotoxicity effects were measured after a 24 and 72 h incubation of both compounds with human breast adenocarcinoma MDA-MB-231 cells. Interestingly, for FAV no pronounced effects on cellular viability were detected neither after 24 nor 72 h incubation in the concentration range of 10–1000 μM (Fig. 11A). In contrast to FAV, DFP exhibits moderate cytotoxic effects on viability of MDA-MB-231 cells after 24 h incubation, but significant inhibition of the cell growth after 72 h treatment (Fig. 11B).

Compared to the untreated control, the cell viability of the MDA-MB-231 cells after 24 h treatment with DFP ranges between 100 % (at 10 μM) and ~ 66 % at the highest tested concentration of 1.0 mM, revealing of a weak cytotoxic effect. However, DFP has shown to inhibit the growth of the MDA-MB-231 cells after 72 h treatment in the concentration range of 250–1000 μM with an IC_{50} of 331.8 ± 68.6 μM, indicating that DFP exhibits pronounced antiproliferative effect on MDA-MB-231 cancer cells (Fig. 11C and 11D).

Next, the ability for drug-drug interactions of FAV and DFP was examined using the ACD/Percepta software tool (ACD/Percepta package version 14.0.0 from Advanced Chemistry Development, Inc., Toronto; Ontario, 2015). According to the prediction, FAV and DFP were predicted to be no inhibitors of the most important CAP1A2, CYP2C9, CYP2C19, CYP2D6, and CYP3A4 enzymes at the highest investigated concentration of 50 μM (*cf.* Table 5). However, additional *in vitro* experiments at higher concentration ranges are required in order to confirm these initial results.

The most important physicochemical and drug-like properties of FAV and DFP including aqueous solubility, the distribution coefficient (cLog*D*) at physiologically relevant pH 7.4, lipophilicity (expressed as cLog*P*), and tPSA, which are key parameters affecting a number of biological effects, were additionally estimated. As summarized in Table 5, DFP showed much higher aqueous solubility (≥11.0 mg/mL at pH7.4) than FAV (<1.0 mg/mL at pH7.4), combined with predicted low lipophilicity values for both compounds (*cf.* Table 5).

In addition to the ADME-T and physicochemical characteristics, the blood–brain barrier (BBB) permeability of FAV, $(FAV)_2Mg$ complex, and DFP was determined using parallel artificial membrane permeability assay (PAMPA). This *in vitro* assay is often used to assess the ability of drugs to penetrate into the brain by passive diffusion in order to predict possible *in vivo* BBB permeability (Kühl et al., 2023; Tzvetkov et al., 2019; Di et al., 2003). The BBB permeability of FAV, $(FAV)_2Mg$, and DFP was measured in ACN, the same solvent as used for the preparation of the FAV–Mg complex, at a concentration of 100 μM after 4 h incubation at room temperature (*cf.* Table 5, Figure S11).

Validation of PAMPA-BBB studies was done by using a set of low (theophylline, designated as –CNS) and high permeable (+CNS) standard drugs (verapamil hydrochloride, quinidine hydrochloride, propranolol hydrochloride, lidocaine, progesterone, and corticosteroide) (for structures, see Fig. S11A). The measured permeability of these standard drugs was then compared with those of the reported (Table S7 and Fig. S11B-C). Comparison of the BBB main permeability (expressed as P_e), determined in this study, revealed that the measured and the reported values for all standard drugs are in good agreement. The plot of reported $-\log P_e$ *vs.* experimental $-\log P_e$ values resulted in a linear regression with a slope of 0.87 (±0.19) and $R^2 = 0.81$ (*cf.* Fig. S11C). The results from the PAMPA-BBB test showed that DFP exhibits low ability to cross BBB by passive diffusion with an effective permeability (expressed as P_e) value of 0.29×10^{-6} cm/s, which is comparable to that observed for theophylline ($P_e = 0.33 \pm 0.02 \times 10^{-6}$ cm/s) (Table 5 and S7).

However, DFP possesses higher BBB permeability compared to FAV and its Mg–complex with P_e values lower than 0.01×10^{-6} cm/s (Table 5, Fig. S11D). According to our results from the PAMPA-BBB study, FAV and DFP can be classified as low and non-permeable compounds, respectively, with negligible ability to cross the BB barrier and thus to enter the brain by transcellular passive diffusion, which can be associated, for example, with reduced possible neurotoxicity (Di et al., 2003). Despite the fact that FAV and DFP are approved drugs with different medical applications, DFP provides better ADME-T properties than FAV, based on the obtained results herein. Therefore, in the light of the very recent phase 3 randomized controlled trial of oral FAV in adult patients (Shah, 2023), we believe that DFP can be considered as a good starting molecule for further development of antiviral drugs, for example, affecting SARS-Cov-2-ACE2 and SARS-Cov-2-M^{pro} proteins combined with its iron chelating activity. In order to validate and to confirm the obtained herein theoretical and experimental data, further *in vitro* and probably *in vivo* investigations with both compared compounds and/or their virtually predicted most active derivatives need to be performed. For example, *in vitro* experiments can be performed using a recombinant expression of SARS-Cov-2-M^{pro} in *E. coli* or studying the binding of each compound of interest to SARS-Cov-2 RBD protein in 293 T cells stably expressing the hACE2 receptor (hACE2/293 T).

Conclusion

In this study, we investigated FAV and DFP as model systems for the design and development of novel antivirals, in particular against COVID-19. The potential of FAV and DFP as basic scaffolds was examined following our *dual virus-host-targeting* approach, including molecular

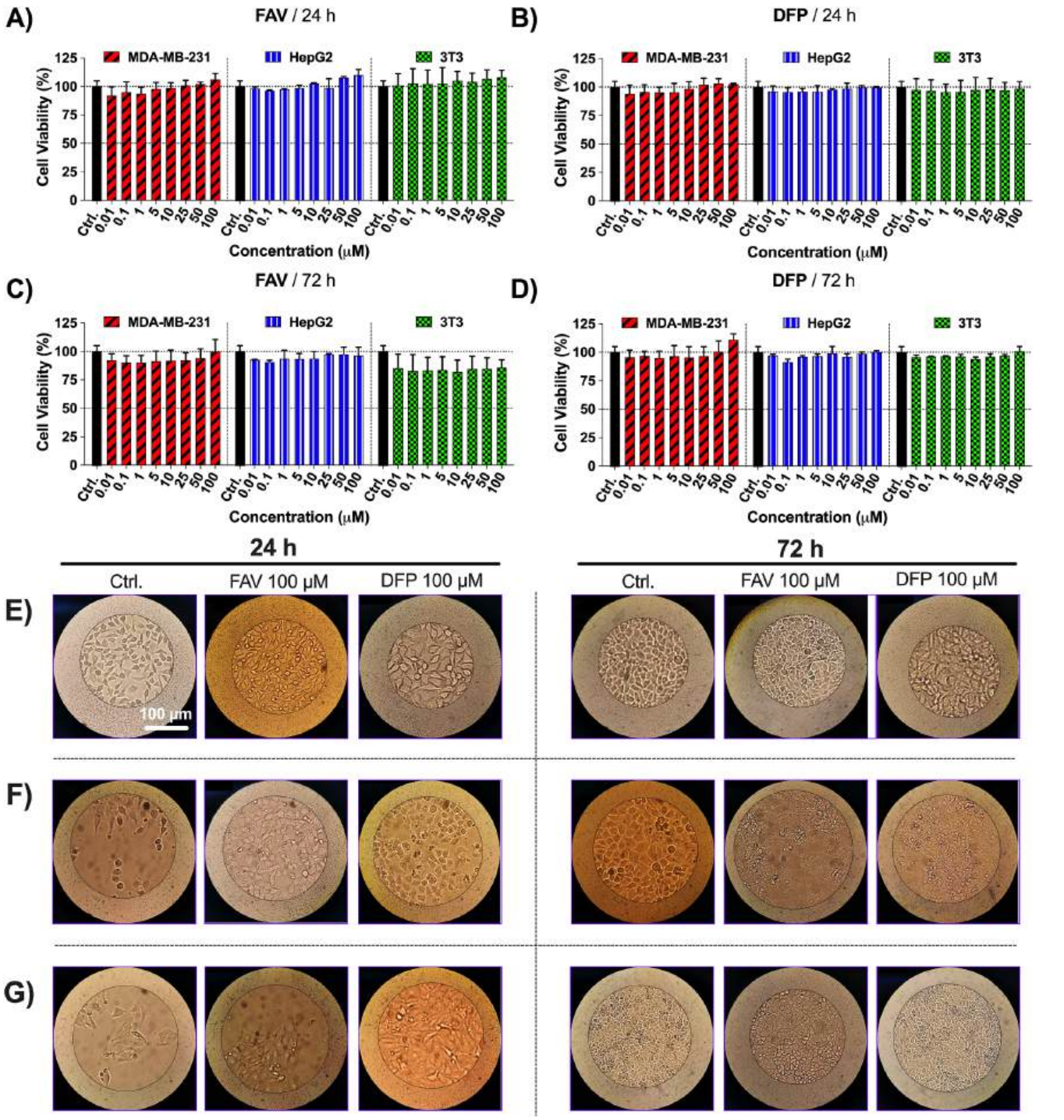

Fig. 10. A–D) Cytotoxicity profile of compounds favipiravir (FAV, **1**) and deferiprone (DFP, **2**) measured on human breast adenocarcinoma MDA-MB-231, human hepatocarcinoma HepG2 and mouse embryonic fibroblasts (3T3) cells after a 24 and 72 h exposure to different low concentrations of compounds (0.01 to 100 μM). E-G) Representative pictures of the respective MDA-MB-231 (E), HepG2 (F) and 3T3 (G) cell cultures after 24 and 72 h treatment with 100 μM of **1** or **2** (100 μm with 20 × magnification). Untreated cells were used as positive control. The results are expressed as the mean % of untreated controls ± SD ($n = 3$). Statistical analysis was performed by one-way ANOVA and Dunnett's multiple comparison test *vs.* the untreated control (Ctrl.).

modeling performed in parallel against two targets of interest – SARS-Cov-2-ACE2 and SARS-Cov-2-M^{pro} – with subsequent tautomer-based drug design and screening for new, virtually active structures. For this purpose, we have investigated the possible tautomers of FAV in comparison with those of DFP by means of quantum-chemical calculations and UV–VISible spectroscopy in different solvents. The calculations and the experiments clearly show the existence only of the enol forms **1E** and **2E** for both compounds in solution, while in the case of FAV, the addition of water shifts the equilibrium partly towards its keto form. The results obtained from the theoretical and the experimental studies indicate that the inhibitory activity of FAV as an RdRd viral inhibitor due to its keto tautomeric form, which appear to be more favorable under physiological conditions. Moreover, we did not observe any evidence for even partial formation of a mixture of two tautomeric forms of DFP (e.g., keto-enol tautomerism) under the herein used experimental conditions. In addition, the chelating activity of DFP to form complexes

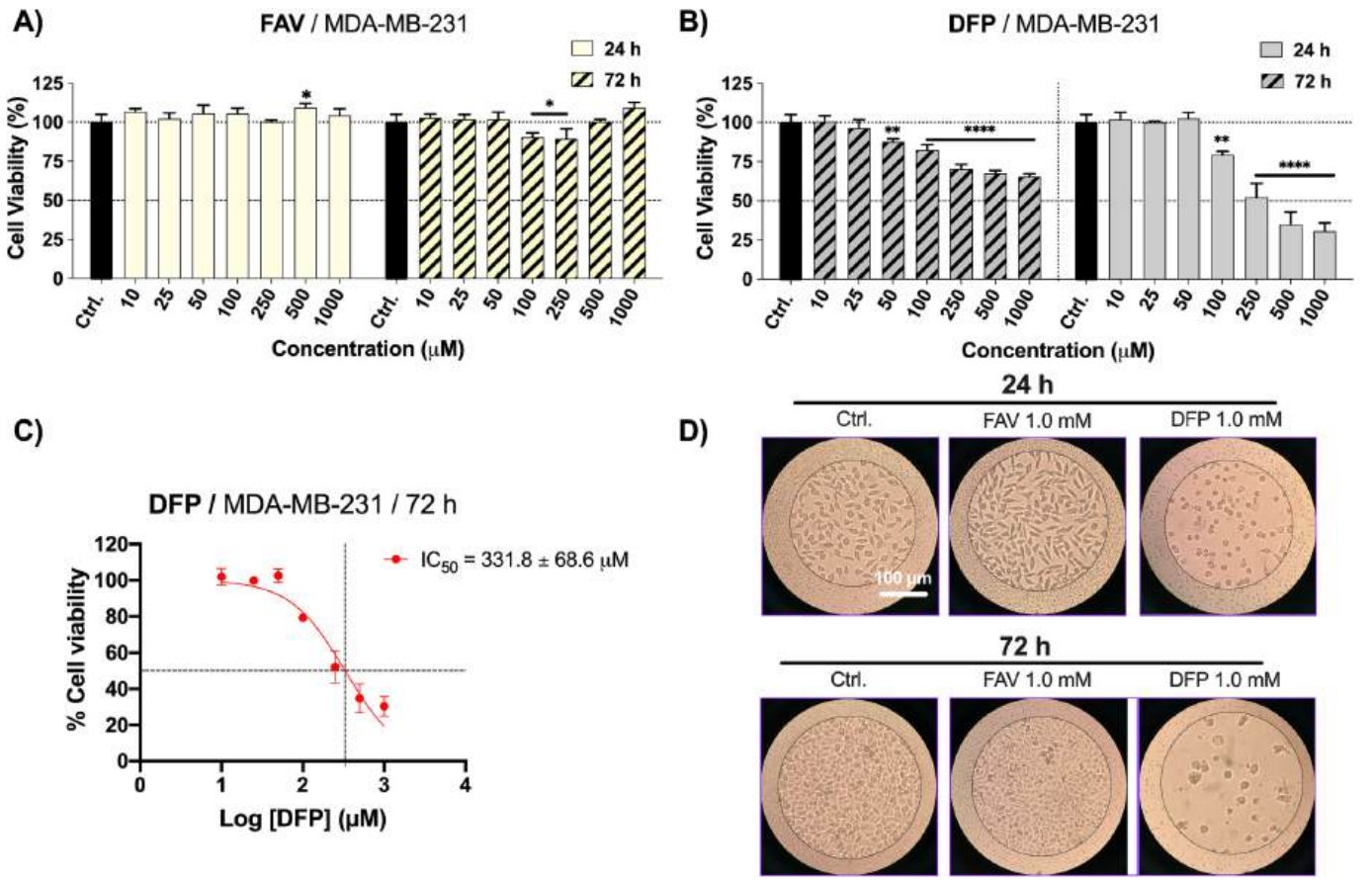

Fig. 11. Cytotoxicity profile of compounds favipiravir (A) (FAV, **1**) and deferiprone (B) (DFP, **2**) measured on human breast adenocarcinoma MDA-MB-231 cells after a 24 and 72 h exposure to different high concentrations of compounds (10 to 1000 μM). C) Nonlinear regression curve of DFP showing the inhibition of MDA-MB-231 cells after 72 h incubation with DEF (the IC_{50} value is indicated). D) Representative pictures of the MDA-MB-231 cell culture after 24 and 72 h treatment with 1000 μM of **1** or **2** (100 μm with 20 × magnification). Untreated cells were used as positive control. The results are expressed as the mean % of untreated controls ± SD ($n = 3$). Statistical analysis was performed by one-way ANOVA and Dunnett's multiple comparison test. *, $p < 0.1$; **, $p < 0.01$; ****, $p < 0.0001$ *vs.* the untreated control (Ctrl.).

with Mg^{2+} in comparison with FAV was evaluated. Our results suggest that quantum-chemical calculations correctly predict the tautomerism in FAV and DFP; as estimated via molecular modeling studies for their biologically active tautomeric forms **1K** and **2E** that were modeled as the best docking poses of FAV and DFP and further used for the design of structures **1a–1c** and **2a–2c** with potential dual activity against SARS-Cov-2-ACE2 and SARS-Cov-2-M^{pro}. The results from virtual screening towards SARS-Cov-2-ACE2 and M^{pro} using the best docking poses of FAV and DFP revealed that both compounds are promising model drugs for tautomer-based drug design of novel small-molecule antivirals against SARS-Cov-2, however, with some preferences to DFP when the results from the ADME-Tox studies are taken into account. Therefore, a combined molecular docking/quantum chemical approach can be recommended in order to obtain well-validated theoretical results in addition to the experiment.

Experimental part

Chemicals

All commercially available anhydrous solvents, reagents, and starting materials were obtained from various producers and used without purification. Favipiravir (**1**, 97 %, CAS#: 259793–96-9, Key Organics/BioNet, Cornwall, UK) and deferiprone (**2**, 98 %, CAS#: 30652–11-0, Santa Cruz Biotechnology Inc., Dallas TX, USA) were used without further purification. All solvents used for spectroscopy measurements were of spectroscopy-grade quality. The complexation studies with favipiravir were performed in acetonitrile as described earlier (Deneva et al., 2023). The complexation of deferiprone with $MgCl_2$ (99.8 %, CAS#: 7786–30-3, ultra-dry, metal basis, AlfaAesar) was studied in acetonitrile (≥99.9 %, CAS#: 75–05-8, LiChrosolv®, Merck). Dry *N*,*N*-dimethylformamide (DMF, 99.8 %, CAS#: 67–64-1, extra dry over molecular sieves, AcroSeal™, Acros) was used throughout the experiments. Ampuwa® water-for-injection (WFI, Fresenius Kabi AG, Bad Homburg von der Höhe, Germany) was applied for preparation of 50 % water mixtures.

Crystallography

Deferiprone (**2**, 4.0 mg) was dissolved in acetonitrile (1.0 mL) under sonification for 10 min. at 40 °C. After three days at room temperature, methanol (1.0 mL) was added to the sample and the mixture was allowed to stay at room temperature until complete evaporation of the sample. Crystals for X-ray structure analysis of compound **2** were grown from methanol (1.0 mL) after slow evaporation of the sample at room temperature to the half of its volume. Single colorless needle crystals of **2** were obtained directly from their mother liqueur containing minimum methanol (0.3–0.5 mL). The crystal data were collected on a Rigaku Supernova diffractometer with Atlas detector using CuKa (λ = 1.54184 Å) radiation at a temperature of 100.0(1) K during data collection. The crystallographic data and refinement results of all structures are given in the Supporting Information. The deposited number CCDC 2258424

contains the supplementary crystallographic data for this paper. These data can be obtained free of charge from The Cambridge Crystallographic Data Centre via https://www.ccdc.cam.ac. uk/data_request/cif.

Molecular modeling studies

Ligand-protein docking

All molecular modeling studies were carried out using the SeeSAR software package (SeeSAR package version 12.1 Narcissus from BioSolveIT GmbH, St. Augustin, 2019), applying the integrated binding site computation and docking modules. For docking experiments, the X-ray structure of the receptor-binding domain (RBD) of the spike protein of SARS-Cov-2 bound to the cell receptor of ACE2 (PDB accession code: 6M0J) (Lan et al., 2020) and the X-ray structure of SARS-Cov-2 main protease (M^{pro}) in complex with the covalently bonded protease inhibitor PF-07321332 (PDB accession code: 7VH8) (Zhao, 2022) were used as input PDB structures for molecular docking studies, pose generation of compounds, visual inspection, scoring, and re-scoring assessment of the representative ligand's best-docked poses. The 3D-struture of favipiravir **1** (ZINC accession code: 000013915654, www.zinc12.docking.org) and the reported single-crystal X-ray structure of deferiprone **2** (CCDC 2258424, www.ccdc.cam.ac.uk) were used as the ligand coordinates input without any further preparation. As recently reported for our docking workflow (Tzvetkov et al., 2017), the X-ray crystallographic structures have led to excellent docking results, usually better than energy-optimized 3D structures of a ligand (e.g., using the MMFF94x force field). The 3D-structure of each ligand was then processed by applying the SeeSAR-integrated docking engine. A maximum of 10 poses was generated for each ligand and target protein to perform post-processing with the HYDE algorithm in SeeSAR. The docking implemented in SeeSAR is based on the FlexX/-SIS algorithms as previously described (Tzvetkov et al., 2017). After visual inspection, the best-ranked docking poses of both ligands were selected and further processing within the binding sites of both proteins, e.g., estimation of binding affinities and binding modes was conducted. In this study, further optimization in terms of (i) torsion/bindings, (ii) intra- and (iii) intermolecular clashes, e.g., by using the molecular editor module in SeeSAR following by re-docking and re-scoring, was not required due to the high quality of the obtained best-scored poses. Therefore, the obtained conformations were used for further computations without further optimizations and saved in SD format data files.

HYDE scoring and visualization

HYDE is a scoring function that is integrated in SeeSAR and, therefore, used to rapidly compute estimates of binding affinities (ΔG) (SeeSAR package version 12.1 Narcissus from BioSolveIT GmbH, St. Augustin, 2019). HYDE considers the hydrogen bonds/salt bridges on the one hand side (roughly interpreted as the ΔH term), and dehydration terms on the other (roughly interpreted as the –TΔS term) (Reulecke et al., 2008; Schneider et al., 2012). Based on that, SeeSAR visualizes the (HYDE-)estimated free energy of binding (ΔG) using translucent spheres (HYDE "coronas") from large, plain red (very unfavorable) to large, plain green coloring (very favorable for affinity). Corona sizes correlate with the amount of contribution of each non-hydrogen atom (Reulecke et al., 2008; Schneider et al., 2012). As output SeeSAR delives further on: (a) the estimated binding affinity (represented as $K_{i\ HYDE}$ ranges), (b) an approximate, respective lipophilic ligand efficiency (LLE_{HYDE}), (c) ligand efficiency (LE), and other relevant physicochemical parameters. Based on the HYDE score, the docked poses of ligands were ranked. Finally, the docking results were visually inspected in terms of their torsional quality by using the assessment of the statistical significance of torsions as implemented in SeeSAR and described previously (Schärfer et al., 2013; Schärfer et al., 2013; TorsionAnalyzer).

Evaluation of tautomerism

The quantum-chemical calculations were performed by using the Gaussian 16 Rev. C.01 program suite (Frisch, 2016). The geometry optimization of the tautomeric forms of both compounds in the ground state was performed by using DFT method at M06-2X/TZVP level of the theory. The M06-2X refers to the range-separated hybrid density functional within the generalized gradient approximation (Zhao and Truhlar, 2008). In our previous studies of tautomeric systems, it has been shown that the selected above functional correctly describes relative stability of the tautomeric forms and demonstrates a good agreement between experimental data and theoretical results (Kawauchi and Antonov, 2013; Antonov et al., 2012; Antonov, 2019). After geometry optimization procedure, the obtained structures were checked for the presence/absence of the imaginary frequency in order to find out the type of the stationary point on potential energy surface (PES). The following energetic characteristics as electronic, zero-point, and thermal free energies were taken into account after geometry optimization and frequency calculations under considering the respective solvent.

Bearing in mind that M06-2X systematically underestimates the absorption band positions (Kawauchi et al., 2014), the UV–VIS spectral data in different solvents were predicted by the B3LYP (Becke, 1993) functional at the same basis set using the M06-2X optimized ground-state geometries ($\Delta\nu_{1/2} = 3500\ cm^{-1}$). All calculations were done taking into account the solvation effects by employing the polarizable continuum model (PCM formalism) (Tomasi et al., 2005), considering acetonitrile as a dielectric medium.

Photophysical studies

UV–VIS spectroscopy

The UV–VIS spectra of FAV and DFP were recorded with a Jasco V-570 UV–VIS/NIR spectrophotometer (Jasco Analytical Instruments Inc., Japan) in 1.0 cm quartz cells in the interval of 200–700 nm with bandwidth of 2.0 nm and scanning speed of 100 nm/min. The spectrophotometer was equipped with a thermostatic cell holder using Huber MPC-K6 thermostat (Peter Huber Kältemaschinenbau AG, Germany) with precision of 1.0 °C. The concentration of the sample was 15 μM for FAV and 30 μM for DFP. The measurements were performed at room temperature in different solvents, as follows: acetonitrile (ACN), toluene, and ACN-water (1:4) for FAV (Deneva et al., 2023), and DMSO, acetonitrile (ACN), methanol (MeOH), DMSO-water (1:1), MeOH–water (1:1), and HEPES buffer (pH 7.4) for compound DFP. A blank sample with the corresponding solvent was used to calibrate the instrument. Recorded UV–VIS spectra were automatically processed and base line corrected.

Metal binding studies

The complexation ability of favipiravir (FAV) with magnesium was measured previously upon stepwise addition of magnesium perchlorate water solutions (Fluka) to an isomolar solution of FAV (15 μM) in acetonitrile (Deneva et al., 2023). The chelating ability of deferiprone (DFP) with metal ions was measured with modifications of previously reported protocol via stepwise titration of magnesium chloride (ultra-dry 99.9 %, metal basis, Alfa Aesar), iron(III) chloride (anhydrous, Alfa Aesar) or iron(III) sulphate heptahydrate (ACS 99+%, Alfa Aesar) water solution (1.0 mM) to an isomolar solution of DFP (30 μM) in acetonitrile (for Mg^{2+}) or in DMSO (for Fe^{3+} and Fe^{2+}) (Tzvetkov and Antonov, 2017). The complexation of **1** with Mg^{2+} and **2** with Fe^{3+}, Fe^{2+} or Mg^{2+} ions was determined by measuring the UV–VIS absorbance spectra of the respective compound in the absence and in the presence of the respective metal salt ($Mg(ClO_4)_2$ for FAV; $FeCl_3$, $FeSO_4$ or $MgCl_2$ for deferiprone), respectively. The UV–VIS experiments were quantified by performing of control experiments with isomolar solutions of each Me^{n+}-salt or each compound alone in acetonitrile or DMSO. All obtained spectra were further analyzed by overlapping the individual spectra that

correspond to the molar fractions in each solution. The logarithmic stability constants for deferiprone of the respective ligand–metal complexes were obtained using the UV–VIS spectroscopic data from at least two independent experiments and calculated with DATAN V.5 software (MultiD Analyses AB, 2013).

PAMPA assay

Determination of blood–brain barrier (BBB) permeability of FAV, DFP, FAV-Mg complex ($Mg(FAV)_2$) and standard drugs was performed using PAMPA Explorer kit (Pion Inc., Billerica, MA, USA) by measuring the UV–VISible absorbance of compounds in both donor and acceptor compartments according to the literature (Kühl et al., 2023; Tzvetkov and Antonov, 2017). Stock solutions of FAV**1** (1.0 mM), DFP (10.0 mM) and $Mg(FAV)_2$ (1.0 mM) were prepared in acetonitrile, while for standard compounds in DMSO (10 mM and 50 mM for theophylline and lidocaine). The corresponding stock solutions were diluted to a final concentration of 100 μM and 50 μM (5.0 μL/well, 1.0 % v/v final DMSO concentration for standard drugs) with pH 7.4 Prisma HT buffer solution in deionized water using a deep-well plate (Pion). The resulting solution (200 μL) was added to each well of the donor plate ($n \geq 6$). The polyvinylidene fluoride filter membrane (PVDF, 0.45 μM) on the acceptor plate was coated with 5.0 μL/well of the GIT-0 lipid (Pion) formulation and placed on the top of the donor plate to form a "sandwich" plate. Then, 200 μL of brain sink buffer (BSB, Pion) was added to each well of the acceptor plate. The "sandwich" plate was incubated in a Good-Box (Pion) at room temperature for 4 h. After that, 150 μL/well of each well of the "sandwich" plates were transferred into the corresponding acceptor and donor plates. A blank UV read 96-well plate with 150 μL/well of each buffer solution was prepared. An Epoch microplate reader was used to obtain the UV–VIS spectra (250–500 nm) of the solutions in the blank, acceptor, and donor plates. The P_e and $-\log P_e$ values for each compound were processed using the PAMPA Explorer software v.3.8 (Pion) and the data are presented as the mean values ± SD of three independent experiments.

Evaluation of cytotoxicity

Cell cultures preparation

Human breast adenocarcinoma (MDA-MB-231), human hepatocellular carcinoma (HepG2), and mouse embryonic fibroblasts (3T3) cells were cultured in Dulbecco's modified Eaglés medium (DMEM, Gibco, Austria) supplemented with 10 % fetal bovine serum (FBS; Gibco, Austria), penicillin (100 U/mL) and streptomycin (0.1 mg/mL) solution (Gibco, USA). All cells were cultured under a humidified CO_2 (5.0 %) atmosphere at 37 °C and passaged by trypsinization when reached approximately 80 % confluence. For experiments, cells in exponential phase of growth (at a density of 0.5×10^5 cells/mL) were seeded into 96-well flat-bottom plates after treatment with trypsin-EDTA (Greiner, Germany) solution at a final volume of 100 μL/well. Cells were incubated overnight before treatment with test substances.

Cell viability assay

The cytotoxicity of FAV (10.0 mM or 100 mM stock solutions in DMSO final concentration 0.05 % DMSO for low concentration tests or with final concentration 0.1 % DMSO for high concentration tests, respectively) and DFP (10 or 100 mM stocks in ddH_2O) was evaluated in the respective cell lines by colorimetric assay using 3-(4,5-dimethylthiazol-2-yl)-2,5-diphenyltetrazolium bromide (MTT) as previously reported (Tzvetkov et al., 2019). Briefly, cells were seeded in 96-well culture plates, treated with the test compounds at different low concentrations (0.01, 0.1, 1.0, 5.0, 10, 25, 50, and 100 μM) or high concentration ranges (10, 25, 50, 100, 250, 500, and 1000 μM) and further incubated for 24 h or 72 h at 37 °C. After incubation period, MTT solution (0.5 mg/mL) was added and cells were incubated for further 180 min. The medium was removed and the plates were placed in a plate shaker at room temperature until complete dissolution of purple formazans. The quantification of formazans produced from the biological sample after reduction of MTT was monitored using a microplate ELISA reader Varioscan™ LUX (Thermo Fisher Scientific Inc., USA) at a wavelength of 550 nm with a reference wavelength of 630 nm. The cytotoxicity of the test peptides determined by MTT assay was expressed as percentage cell viability according to the following equation:

$$\%\text{Cell viability} = (A_{sample} - A_{blank})/(A_{control} - A_{blank}) \times 100.$$

In this equation, A_{sample}, A_{blank} and $A_{control}$ are the measured absorption of the respective test sample, blank solution, and control sample. The results were expressed as the mean % of the untreated controls ± SD from three independent experiments ($n = 3$).

Statistical analysis

All graphs and the statistical analysis were performed using GraphPad Prism 9.0 (GraphPad Software, La Jolla, CA, USA). The IC50 value for DFP inhibition of MDA-MB-231 cells at 72 h was obtained by nonlinear regression using the equation log(inhibitor) *vs.* normalized response – variable slope and expressed as mean ± standard deviation (SD) of the untreated control. Normalization of the raw data was performed to the untreated control data (100 ± 5.0 %). The data from the MTT tests were analyzed using one-way ANOVA followed by a Dunnett's multiple comparison test to compare the drug (FAV and DFP) with the untreated control (Ctrl.) group. A difference between the groups was considered significant at *p*-values (* $p < 0.1$, ** $p < 0.01$ and **** $p < 0.0001$ *vs.* Ctrl.).

Funding Sources

This work was funded by the Bulgarian National Science Fund (BNSF) under research grant KP-06-COST/1 (COST Action CA18202).

CRediT authorship contribution statement

Nikolay T. Tzvetkov: Conceptualization, Software, Visualization, Validation, Writing – original draft, Funding acquisition, Project administration, Supervision, Resources. **Martina I. Peeva:** Validation. **Maya G. Georgieva:** Validation, Supervision. **Vera Deneva:** Data curation, Methodology. **Aneliya A. Balacheva:** Methodology. **Ivan P. Bogdanov:** Validation. **Maria Ponticelli:** Writing – review & editing. **Luigi Milella:** Writing – review & editing. **Kiril Kirilov:** Software, Visualization. **Maima Matin:** Writing – review & editing. **Hans-Georg Stammler:** Methodology, Software, Data curation, Writing – review & editing. **Atanas G. Atanasov:** Writing – review & editing, Supervision. **Liudmil Antonov:** Methodology, Data curation, Writing – review & editing, Supervision.

Declaration of competing interest

The authors declare the following financial interests/personal relationships which may be considered as potential competing interests: [Nikolay Tzvetkov Tzvetkov reports financial support was provided by Bulgarian National Science Fund. If there are other authors, they declare that they have no known competing financial interests or personal relationships that could have appeared to influence the work reported in this paper].

Data availability

No data was used for the research described in the article.

Acknowledgments

The financial support from the Bulgarian National Science Fund (project KP-06-COST/1, COST Action CA18202) is gratefully acknowledged.

Appendix A. Supplementary data

Supplementary data to this article can be found online at https://doi.org/10.1016/j.crbiot.2024.100176.

References

TorsionAnalyzer was developed in collaboration between F. Hoffmann-LaRoche, Switzerland, and the Center for Bioinformatics (ZBH) of the University of Hamburg; http://www.biosolveit.de/TorsionAnalyzer/.

ACD/Percepta package version 14.0.0 from Advanced Chemistry Development, Inc., Toronto; Ontario 2015, Canada (www.acdlabs.com).

Anighoro, A., Bajorath, J., Rastelli, G., 2014. Polypharmacology: challenges and opportunities in drug discovery. J. Med. Chem. 57 (19), 7874–7887.

Antonov, L., 2019. Tautomerism in azo and azomethyne dyes: when and if theory meets experiment. Molecules 24, 2252].

Antonov, L., 2020. Favipiravir tautomerism: A short theoretical report. Cambridge Open Engage, ChemRxiv, Cambridge.

Antonov, L., 2020. Favipiravir tautomerism: A theoretical insights. Theor. Chem. Acc. 139, 145.

Antonov, L., Kurteva, V., Crochet, A., Mirolo, L., Fromm, K.M., Angelova, S., 2012. Tautomerism in 1-phenylazo-4-naphthols: Experimental results vs. quantum-chemical predictions. Dyes Pigments. 92, 714–723.

Aronskyy, I., Masoudi-Sobhanzadeh, Y., Cappuccio, A., Zaslavsky, E., 2021. Advances in the computational landscape for repurposed drugs against COVID-19. Drug Discov. Today 26 (12), 2800–2815.

Becke, A.D., 1993. Density-functional thermochemistry. III. The role of exact exchange. J. Chem. Phys. 98, 5648–5652.

Beigel, J.H., et al., 2020. ACTT-1 Study Group Members, Remdesevir for the treatment of Covid-19 – Final report. N. Engl. J. Med. 383 (19), 1813–1826.

Choudhary, S., Malik, Y.S., Tomar, S., 2020. Identification of SARS-Cov-2 cell entry inhibitors by drug repurposing using *in silico* structure-based virtual screening approach. Front. Immunol. 11, Article 1664.

Cilibrizzi, A., Abbate, V., Chen, Y.-L., Ma, Y., Zhou, T., Hider, R.C., 2018. Hydroxypyridinone journey into metal chelation. J. Med. Chem. 118, 7657–7701.

Deneva, V., Slavova, S., Kumanova, A., Vassilev, N., Nedeltcheva-Antonova, D., Antonov, L., 2023. Favipiravir-tautomeric and complexation properties in solution. Pharmaceuiticals 16, 45.

Di, L., Kerns, E.H., Fan, K., McConnell, O.J., Carter, G.T., 2003. High throughput artificial membrane permeability assay for blood-brain barrier. Eur. J. Med. Chem. 38, 223–232.

Du, Y.-X., Chen, X.-P., 2020. Favipiravir: Pharmacokinetics and concerns about clinical trials for 2019-nCoV infection. Clin. Pharmacol. Ther. 108 (2), 242–247.

Entezari, S., et al., 2022. Iron chelators in treatment of iron overload. J. Toxicol. 4911205, 18 pages.

Esmel-Vilomara, R., et al., 2022. QTc interval prolongation in patients infected with SARS-Cov-2 and treated with antiviral drugs. An. Pediatr. 96, 213–220.

Frisch, M.J., et al., Gaussian 16 Revision C.01, Gaussian Inc.: Wallingford, CT, USA, 2016.

Futura, Y., Gowen, B.B., Takahashi, K., Shiraki, K., Smee, D.F., Barnard, D.L., 2013. Favipiravir (T-705), a novel viral RNA polymerase inhibitor. Antivir. Res. 100 (2), 446–454.

Galindez, G., Matschinske, J., Rose, T.D., Sadegh, S., Salgado-Albarrán, M., Späth, J., Baumbach, J., Pauling, J.K., 2021. Lessons from the COVID-19 pandemic for advancing computational drug repurposing. Nat. Comput. Sci. 1, 33–41.

Ghosh, A.K., Brindisi, M., Shahabi, D., Chapman, M.E., Mesecar, A.D., 2020. Drug development and medicinal chemistry efforts toward SARS-coronavirus and Covid-19 therapeutics. ChemMedChem 15 (11), 907–932.

Gil, C., Ginex, T., Maestro, I., Nozal, V., Barrado-Gil, L., Cuesta-Geijo, M.A., Urquiza, J., Ramiret, D., Alonso, C., Campillo, N.E., Martinez, A., 2020. COVID-19: Drug targets and potential treatments. J. Med. Chem. 63 (21), 12359–12386.

Good, S.S., Westover, J., Jung, K.H., Zhou, X.-J., Moussa, A., La Colla, P., Collu, G., Canard, B., Sommadossi, J.-P., 2021. AT-527, a double prodrug of a guanosine nucleotide analog, is a potent inhibitor of SARS-Cov-2 *in vitro* and a promising oral antiviral for treatment of COVID-19. Antimicrob. Agents Chemother. 65 (4), e02479–e10520.

Gunaydin-Alkyildiz, A., Aksoy, N., Boran, T., Ilhan, E.N., Ozhan, G., 2022. Favipiravir induces oxidative stress and genotoxicity in cardiac and skin cells. Toxicol. Lett. 371, 9–16.

Habib, H.M., Ibrahim, S., Zaim, A., Ibrahim, W.H., 2021. The role of iron in the pathogenesis of COVID-19 and possible treatment with lactoferrin and other iron chelators. Biomed. Pharmacother. 136, 111228.

Halford, B., 2021. Pfizer unveils its oral SARS-Cov-2 inhibitor. C&EN 99 (13), 7.

Hammond, J., et al., 2022. Oral nirmatrelvir for high-risk, nonhospitalized adults with Covid-19. N. Engl. J. Med. 386 (15), 1397–1408.

Holman, W., et al., 2021. Accelerated first-in-human clinical trial of EIDD-2801/MK4482 (molnupiravir), a ribonucleoside analog with potent antiviral activity against SARS-Cov-2. Trials 22, 561.

Hu, X., Chen, C.Z., Xu, M., Hu, Z., Guo, H., Itkin, Z., Shinn, P., Ivin, P., Leek, M., Liang, T. J., Shen, M., Zheng, W., Hall, M.D., 2021. Discovery of small molecule entry inhibitors targeting the fusion paptide of SARS-Cov-2 spike protein. ACS Med. Chem. Lett. 12 (8), 1267–1274.

Hufsky, F., et al., 2021. Computational strategies to combat COVID-19: useful tools to accelerate SARS-Cov-2 and coronavirus research. Briefings Bioinf. 22 (2), 642–663.

Jin, Z., et al., 2020. Structure of M^{pro} from SARS-Cov-2 and discovery of its inhibitors. Nature 582, 289–293.

Jin, Z., Smith, L.K., Rajwanshi, V.K., Kim, B., Deval, J., 2013. The ambiguous base-paring and high substrate efficiency of T-705 (favipiravir) ribofuranosyl 5'-triphosphate towards influence A virus polymerase. PloS One 8 (7), e68347.

Jin, Z., Smith, L.K., Rajwanshi, V.K., Kim, B., Deval, J., 2013. The ambiguous base-pairing and high substrate efficiency of T-705 (Favipiravir) ribofuranosyl 5'-triphosphate towards influenza A virus polymerase. PlosOne 8 (7), e68347.

Kawauchi, S., Antonov, L., 2013. Description of the Tautomerism in Some Azonaphthols: description of the tautomerism in some azonaphtols. J. Phys. Org. Chem. 26, 643–652.

Kawauchi, S., Antonov, L., Okuno, Y., 2014. Prediction of the color of dyes by using time-dependent density functional theory. Bulg. Chem. Commun. 46, 228–237.

Kontoghiorghes, G.J., 2022. Deferiprone: A forty-year-old multi-targeting drug with possible activity against COVID-19 and diseases of similar symptomatology. Int. J. Mol. Sci. 23, 6735.

Kontoghiorghes, G.J., Kontoghiorghe, C.N., 2020. Iron and chelation in biochemistry and medicine: new approaches to controlling iron metabolism and treating related disease. Cells 9, 1456.

Kostadinova, I.D., Andronova, V.L., Fateev, I.V., Esipov, R.S., 2022. Favipiravir and its structural analogs: Antiviral activity and synthesis methods. Acta Nat. 14, 16–38.

Kühl, T., Georgieva, M.G., Hübner, H., Lazarova, M., Vogel, M., Haas, B., Peeva, M.I., Balacheva, A.A., Bogdanov, I.P., Milella, L., Ponticelli, M., Garev, T., Faraone, I., Detcheva, R., Minchev, B., Petkova-Kirova, P., Tancheva, L., Kalfin, R., Atanasov, A. G., Antonov, L., Pajpanova, T.I., Kirilov, K., Gastreich, M., Gmeiner, P., Imhof, D., Tzvetkov, N.T., 2023. Neurotensin(8–13) analogs as dual NTS1 and NTS2 receptor ligands with enhanced effects on a mouse model of Parkinson's disease. Eur. J. Med. Chem. 254, 115386.

Kupferschmidt, K., Cohen, J., 2020. Race to find COVID-19 treatments accelerates. Science 367 (6485), 1412–1413.

Lan, J., Ge, J., Yu, J., Shan, S., Zhou, H., Fan, S., Zhang, Q., Shi, X., Wang, Q., Zhang, L., Wang, X., 2020. Structure of the SARS-Cov-2 spike receptor-binding domain bound to the ACE2 receptor. Nature 581, 215–220.

Li, X., Li, X., Liu, F., Li, S., Shi, D., 2021. Rational multitargeted drug design strategy from the perspective of a medicinal chemist. J. Med. Chem. 64 (15), 0581–10605.

Liu, W., Li, H., 2020. COVID-19: Attacks the 1-beta chain of hemoglobin and captures the porphyrin to inhibit human heme metabolism. Cambridge Open Engage, ChemRxiv, Cambridge.

Liu, C.-H., Lu, C.-H., Wong, S.H., Lin, L.-T., 2021. Update on antiviral strategies against COVID-19: Unmet needs and prospects. Front. Immunol. 11, 616595.

Maas, M.N.J., Hintzen, C.J., Löffler, P.M.G., Mecinovic, J., 2021. Targeting SARS-Cov-2 spike protein by stapled hACE2 peptides. Chem. Commun. 57, 3283–3286.

Michaud, V., Dow, P., Al Rihani, S.B., Deodhar, M., Arwood, M., Cicali, B., Turgeon, J., 2021. Risk assessment of drug-induced long QT syndrome for some COVID-19 repurposed drugs. Clin. Transl. Sci. 14, 20–28.

Pozzi, C., Vanet, A., Francesconi, V., Tagliazucchi, L., Tassone, G., Venturelli, A., Spyrakis, F., Mazzorana, M., Costi, M.P., Tonelli, M., 2023. Antitarget, anti-SARS-CoV2 leads, drugs, and the drug discovery-genetics alliance perspective. J. Med. Chem. 66 (6), 3664–3702.

Rattanaumpawan, P., Jirajariyavej, S., Lerdlamyong, K., Palavutitotai, N., Saiyarin, J., 2022. Real-world effectiveness and optimal dosage of favipiravir for treatment of COVID-19: results from a multicenter observational study in Thailand. Antibiotics 11, 805.

Reulecke, I., Lange, G., Albrecht, J., Klein, R., Rarey, M., 2008. Towards an Integrated Description of Hydrogen Bonding and Dehydration: Decreasing False Positives in Virtual Screening with the HYDE Scoring Function. ChemMedChem 3 (6), 885–897.

Sadremomtaz, A., Al-Dahmani, Z., Ruiz-Moreno, A., Monti, A., Wang, C., Azad, T., Bell, J. C., Doti, N., Velasco-Velázquez, M.A., de Jong, D., de Jonge, J., Smit, J., Dömling, A., van Goor, H., Groves, M.R., 2022. Peptides that antagonize the angiotensin-converting enzyme-2 (ACE-2) infection with SARS-Cov-2 receptor binding. J. Med. Chem. 65 (4), 2836–2847.

Schärfer, C., Schulz-Gasch, T., Ehrlich, H.C., Guba, W., Rarey, M., Stahl, M., 2013. Torsion angle preferences in drug-like chemical space: A comprehensive guide. J. Med. Chem. 56, 2016–2028.

Schärfer, C., Schulz-Gasch, T., Hert, J., Heinzerling, L., Schulz, B., Inhester, T., Stahl, M., Rarey, M., 2013. CONFECT: Conformations from an expert collection of torsion patterns. ChemMedChem. 8, 1690–1700.

Schneider, N., Hindle, S., Lange, G., Klein, R., Albrecht, J., Briem, H., Beyer, K., Claußen, H., Gastreich, M., Lemmen, C., Rarey, M., 2012. Substantial improvements in large-scale redocking and screening using the novel HYDE scoring function. J. Comput.-Aided Mol. Des. 12, 701–723 and references therein.

Schneider, N., Lange, G., Hindle, S., Klein, R., Rarey, M., 2013. A consistent description of HYdrogen bond and DEhydration energies in protein-ligand complexes: methods behind the HYDE scoring function. J. Comput. Aided Mol. Des. 27, 15–29.

SeeSAR package version 12.1 Narcissus from BioSolveIT GmbH, St. Augustin 2019, Germany (http://www.biosolveit.de/SeeSAR).

Shah, P.L., et al., 2023. Favipiravir in patients hospitalized with COVID-19 (PIONEER trial): a multicentre, open-label, phase 3, randomized controlled trial of early intervention versus standard care. The Lancet 11 (5), 415–424.

Shiraki, K., Daikoku, T., 2020. Favipiravir, an anti-influenza drug against life-threating RNA virus infections. Pharmacol. Ther. 209, 107512.

Shur, Z.A., Gorshkov, K., Chen, C.Z., Zheng, W., 2020. Drug discovery strategies for SARS-Cov-2. J. Pharmacol. Exp. Ther. 375 (1), 127–138.

Tai, W., Zhang, X., He, Y., Jiang, S., Du, L., 2020. Identification of SARS-Cov RBD-targeting monoclonal antibodies with cross-reactive or neutralizing activity against SARS-Cov-2. Antivir. Res. 179, 104820.

Tomasi, J., Mennucci, B., Cammi, R., 2005. Quantum Mechanical Continuum Solvation Models. Chemical Reviews. 105, 2999–3094.
Tzvetkov, N.T., Antonov, L., 2017. Subnanomolar indazole-5-carboxamide inhibitors of monoamine oxidase B (MAO-B) continued: indications of iron binding, experimental evidence for optimized solubility and brain penetration. J. Enz. Inh. Med. Chem. 32, 960–967.
Tzvetkov, N.T., Neumann, B., B., Stammler, H.-G., Antonov, L., 2016. A simple approach to multifunctionalized N1-alkylated 7-amino-6-azaoxindole derivatives using their *in situ* stabilized tautomer form. Tetrahedron 72 (41), 6455–6466.
Tzvetkov, N.T., Stammler, H.-G., Neumann, B., Hristova, S., Antonov, L., Gastreich, M., 2017. Crystal structures, binding interactions, and ADME evaluation of brain penetrant N-substituted indazole-5-carboxamides as subnanomolar, selective monoamine oxidase B and dual MAO-A/B inhibitors. Eur. J. Med. Chem. 127, 470–492.
Tzvetkov, N.T., Stammler, H.-G., Georgieva, M.G., Russo, D., Faraone, I., Balacheva, A. A., Hristova, S., Atanasov, A.G., Milella, L., Antonov, L., Gastreich, M., 2019. Carboxamides vs. methanimines: Crystal structures, binding interactions, photophysical studies, and biological evaluation of (indazole-5-yl)methanimines as monoamine oxidase B and acetylcholinesterase inhibitors Eur. J. Med. Chem. 179, 404–422.
V'kovski, P., Kratzel, A., Steiner, S., Stalder, H., Thiel, V.,, 2021. Coronavirus biology and replication: implications for SARS-Cov-2. Nat. Rev. Microbiol. 19, 155–170.
VanPatten, S., He, M., Altiti, A., Cheng, K.F., Ghanem, M.H., Al-Abed, Y., 2020. Evidence supporting the use of peptides and peptidomimetica as potential SARS-Cov-2 (COVID-19) therapeutics. Future Med. Chem. 12 (18), 1647–1656.
Wang, M., et al., 2020. Remdesivir and chloroquine effectively inhibit the recently emerged novel coronavirus (2019-nCoV) in vitro. Cell Res. 30, 269–271.
Wang, T., Fang, X., Wen, T., Liu, J., Zhai, Z., Wang, Z., Meng, J., Yang, Y., Wang, C., Xu, H., 2021. Synthetic neutralizing peptides inhibit the host cell binding of spike protein and block infection of SARS-Cov-2. J. Med. Chem. 64 (19), 14887–14894.
Wang, D., Huang, J., Yeung, A.W.K., Tzvetkov, N.T., Horbanczuk, J.O., Willschke, H., Gai, Z., Atanasov, A.G., 2020. The significance of natural product derivatives and traditional medicine for COVID-19. Processes 8 (8), 937.
Wang, D., Huang, J., Yeung, A.W.K., Tzvetkov, N.T., Horbanczuk, J.O., Willschke, H., Gai, Z., Atanasov, A.G., 2020. The significance of natural product derivatives and traditional medicine for COVID-19. Processes 8 (8), 937.
Willyard, C., 2021. How antiviral pill molnupiravir shot ahead in the COVID-drug hunt, Nature News 08 October.
Wrapp, D., Wang, N., Corbett, K.S., Goldsmith, J.A., Hsieh, C.-L., Abiona, O., Graham, B. S., McLellan, J.S., 2020. Cryo-EM structure of the 2019-nCoV spike in the perfusion conformation. Science 367 (6483), 1260–1263.
Xue, X., et al., 2007. Production of authentic SARS-Cov M(pro) with enhanced activity: Application as a novel tag-cleavage endopeptidase for protein overproduction. J. Mol. Biol. 366 (3), 965–975.
Yan, R., Zhang, Y., Li, Y., Xia, L., Guo, Y., Zhou, Q., 2020. Structural basis for the recognition of SARS-Cov-2 by full-length human ACE2. Science 367 (6485), 1444–1448.
Zhang, L., Lin, D., Sun, X., Curth, U., Drosten, C.h., Sauerhering, L., Becker, S., Rox, K., Hilgenfeld, R., 2020. Crystal structure of SARS-Cov-2 main protease provides a basis for design of improved α-ketoamide inhibitors. Science 368 (6489), 409–412.
Zhao, Y., et al., 2022. Crystal structure of SARS-CoV-2 main protease in complex with protease inhibitor PF-07321332. Protein & Cell 13, 689–693.
Zhao, Y., Truhlar, D.G., 2008. The M06 suite of density functionals for main group thermochemistry, thermochemical kinetics, noncovalent interactions, excited states, and transition elements: two new functionals and systematic testing of four M06-class functionals and 12 other functionals. Theor. Chem. Acc. 120, 215–241.
Zhuravel, S.V., et al., 2021. Nafamostat in hospitalized patients with moderate to severe COVID-19 pneumonia: a randomized Phase II clinical trial. Eclnical Medicine 41, 101169.